

# VLHC Accelerator Physics

Version 0.2 March 19, 2001

## Contents

<b>1</b>	<b>MACHINE LAYOUTS</b>	<b>2</b>
1.1	Overview: 2 colliders in 1 tunnel (Syphers)	2
1.2	Footprint and optical modules (Peggs)	2
1.2.1	Half cell length	3
<b>2</b>	<b>PHASE I: THE LOW-FIELD RING (Syphers)</b>	<b>8</b>
2.1	Lattice (Johnstone)	8
2.2	Magnet aperture and field quality (Sen)	10
2.2.1	Scaling the Main Injector errors	10
2.2.2	Dynamic aperture at injection	11
2.2.3	Dynamic aperture at collision	14
2.3	Tolerances (Sen)	16
2.4	Corrections	16
2.4.1	Closed orbit (Michelotti)	16
2.4.2	Other (Sen)	16
2.5	Stability issues (Ng)	16
2.5.1	Resistive wall	16
2.5.2	Potential-well distortion	17
2.5.3	Longitudinal mode-coupling instability	18
2.5.4	Transverse mode-coupling instability	18
2.5.5	Other issues	19
2.6	Polarization discussion (Vogt)	19
2.7	Beam transfer from low field to high field (Gelfand)	19
<b>3</b>	<b>PHASE II: THE HIGH-FIELD RING</b>	<b>20</b>
3.1	Operational scenarios (Peggs)	20
3.1.1	The head on beam-beam interaction	23
3.1.2	Crossing angles and parasitic beam-beam collisions.	25
3.1.3	Intra beam scattering and diffusion	27
3.1.4	Luminosity versus energy	27
3.2	Lattice optics (Tepikian)	29
3.3	Magnet aperture and field quality (Fischer)	36
3.4	Tolerances (Ptitsyn)	39
3.4.1	Orbit errors	39
3.4.2	Tune error, coupling and IR chromatic effects	39
3.4.3	Tolerance summary	40
3.5	Corrections (Pilat)	40
3.5.1	Arc correction system	41
3.5.2	Interaction region correction system	41
3.6	Beam stability (Blaskiewicz)	42
3.7	Synchrotron radiation (Trbojevic)	47
3.8	Electron cloud instability (Zhang)	50
3.9	Energy deposition (Drees)	50
3.10	Parameter tables	53
3.11	Magnet reference harmonics	58
<b>4</b>	<b>GROUND MOTION AND EMITTANCE GROWTH (Shiltsev)</b>	<b>62</b>

# 1 MACHINE LAYOUTS

## 1.1 Overview: 2 colliders in 1 tunnel (Syphers)

## 1.2 Footprint and optical modules (Peggs)

Both low field and high field ring lattices are constructed from optical modules placed end to end like lego blocks. Each optical module – an arc, dispersion suppressor, interaction region straight, et cetera – has an overall length which is an integer multiple of  $L_{hc}$ , the arc half cell length. Low and high field modules with the same function can be quite different in implementation. For example, the low field arc half cell contains 2 combined function bending magnets, while the high field arc half cell contains 7 pure dipoles. Nonetheless, optical modules in both low field and high field rings always have the same overall length and the same bending angle. For example, in both low and high field rings a Dispersion Suppressor module is 3  $L_{hc}$  long, constructed from 4 dispersions suppressor half cells of length  $3/4 L_{hc}$ , each with  $2/3$  of the bending of a regular arc half cell.

Circumference, $C$	233.037	km
Average arc radius	35.0	km
Half cell length, $L_{hc}$	135.486	m
Half cell bend angle	3.875	mrاد
Half cell count	1720	
Half cell harmonic	24	
Bunch spacing (53.1 MHz)	5.645	m
Number of buckets	41280	
Phase advance per cell	90.0	deg
Revolution frequency	1.286	kHz
Harmonic number	371520	
RF frequency ( $9 \times 53.1$ )	478.0	MHz

Table 1: Fundamental lattice parameters common to both low and high field rings.

Table 1 lists the fundamental parameters of the VLHC footprint, as used in the Feasibility Study [1]. Table 2 lists the sequence of optical modules for half the ring – one arc and the utility region on the Fermilab site – in mnemonic form, using short aliases such as “IR” for the Interaction Region modules, “DM” for the Dispersion Modules and “IA” for the Injection/Abort straight. The footprint geometry for the off-site utility region, half way around the VLHC, is identical. The two utility regions are separated by identical arcs. Table 3 lists the sequence of optical modules in the on-site utility region in greater detail, including the key for the mnemonics.

Figure 1 shows a scale layout of the optical modules in the on-site utility region, including 2 interaction points (IPs). Injection from the Tevatron is naturally away from the 2 IPs, since the VLHC is about 100 meters below the ground surface. One of the two abort lines per ring is shown, missing the neighboring IP by about 40 meters. A common abort dump area is possible for the four beams, approximately 100 meters from the horizontal crossing point “X” of the low field ring. Figure 1 also shows that the muon plume emanation from one IP misses the other experiment by approximately 70 meters.

One advantage of modular construction is that low and high field lattices are guaranteed to have almost identical footprints, and therefore to fit in the same tunnel, so long as corresponding low and high field modules are placed on top of each other. Figure 2 shows the transverse offset of the high field ring relative to the low field ring. The maximum deviation is only about ?? mm, easily allowing one ring to be placed on top of the other at all locations in the VLHC tunnel.

Module	Arc	DS	IA	DM8	IR	DM	X	DM	IR	DM8	IA	DS
$L/L_{hc}$	780	3	10	8	12	6	2	6	12	8	10	3

Table 2: Sequence of optical modules around half of the VLHC (mnemonic version).

MODULE	ALIAS	$L/L_{hc}$	COMMENT
Dispersion Suppressor	DS	3	
Injection/Abort straight	IA	10	
Dispersion Module	DM8	8	contains 2 arc half cells
Interaction Region	IR	12	
Dispersion Module	DM	6	
Crossing “straight”	X	2	
Dispersion Module	DM	6	
Interaction Region	IR	12	
Dispersion Module	DM8	8	contains 2 arc half cells
Injection/Abort straight	IA	10	
Dispersion Suppressor	DS	3	
Utility total		80	
Arc		780	
GRAND TOTAL		1720	2 arcs plus 2 utilities

Table 3: Sequence of optical modules in the on-site utility region of the VLHC.

In the transition from Phase I to Phase II operation, the experiments will remain centered on the same interaction points. (At the same time it is envisaged that they will be upgraded to take up more space along the beam line, increasing the distance from the IP to the first magnet,  $L^*$ , from 20 to 30 m.) It is therefore necessary to add a bypass to keep the low field ring beams well clear of the experiments. This must be done without changing the total low field ring circumference. Figure 3 is a cartoon of a “proof-of-principle” bypass which will work, but which has not been designed in any detail. The total length of the bypass is approximately 8 km in its present incarnation.

### 1.2.1 Half cell length

The average bending radius of the arcs is made as close as possible to the goal value of  $R = 35$  km by adjusting the total equivalent number of (bending) arc cells in each ring. Each of the 4 short half cells in each dispersion suppressor has 2/3 the bending of an arc half cell. Thus, the 20 dispersion suppressors (on either side of 10 straights) have a total bending equivalent to 160/3 arc half cells. If there are  $N = 784$  arc half cells in each half of the VLHC, then the bend per half cell is

$$\theta = \frac{2\pi}{2N + 160/3} = 3.875 \text{ [mrad]} \quad (1)$$

and the average arc bend radius is

$$R = \frac{L_{hc}}{\theta} = 34.961 \text{ [km]} \quad (2)$$

Why is the nominal arc half cell length of  $L_{hc} = 135.4865$  m? Is it close to an optimum? What other lengths are possible?

An important advantage of modular design is the ability to independently modify one particular module without adjusting any other modules. For example, it is possible to increase or decrease the length of a module in quanta of  $L_{hc}$  while (almost) trivially maintaining optical matching conditions. Such length modifications will not disturb the bunch spacing – or the injection scheme or the RF system, et cetera – if the arc half cell length is an integer times the minimum allowed bunch spacing. In this case the total circumference is guaranteed to correspond to an integer number of evenly spaced bunches. The (minimum) bunch spacing  $S_B$  is taken to be one 53.1 MHz RF wavelength in the Tevatron

$$S_B = \lambda_{53} \equiv \frac{2,000\pi}{1113} = 5.645 \text{ meters} \quad (3)$$

This guarantees that the filling schemes from the Tevatron will be relatively simple. The bunch time spacing of about 18.8 ns is not unreasonably challenging to the experiments.

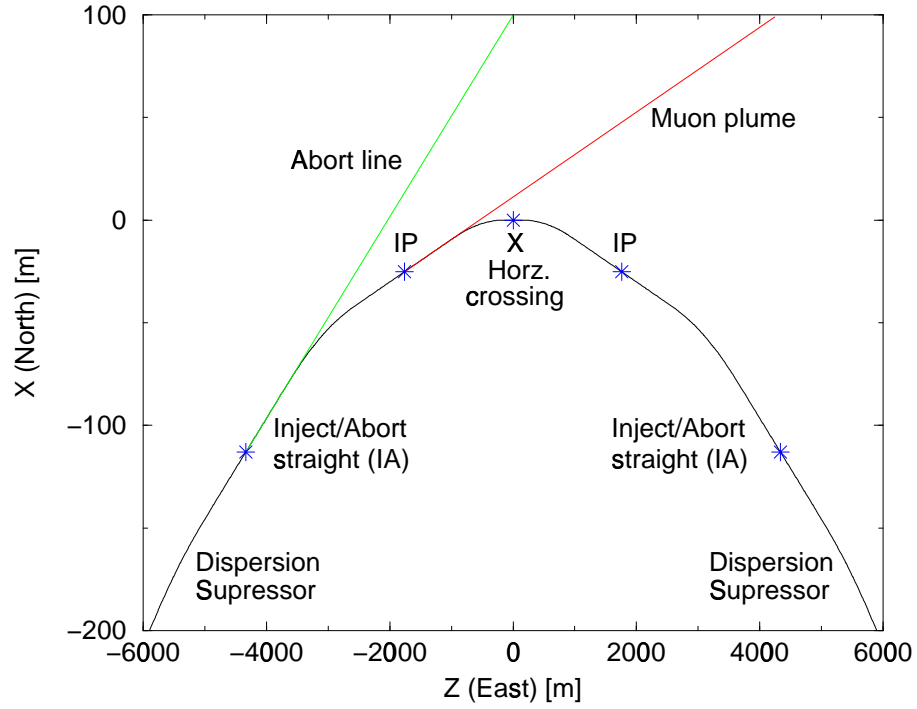


Figure 1: Scale layout of the on-site utility region of the VLHC, showing the clearance of abort lines and muon plumes from the experiments, and suggesting the use of a common abort dump area.

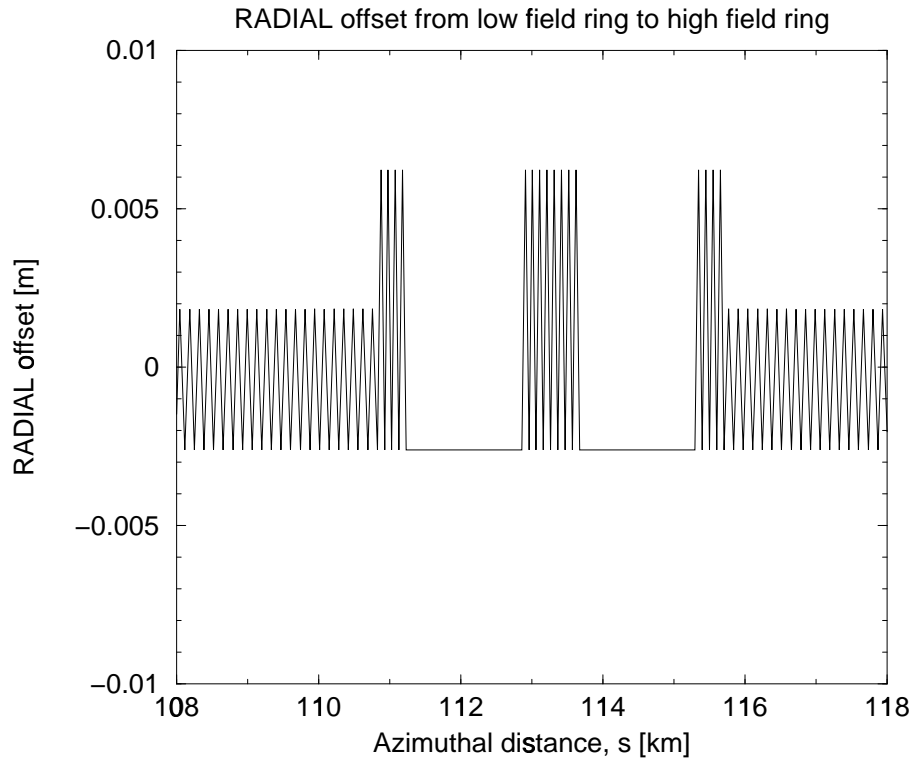


Figure 2: The transverse offset of the high field ring, relative to the low field ring. Both rings easily fit in the same tunnel. (THIS FIGURE NEEDS TO BE UPDATED.)

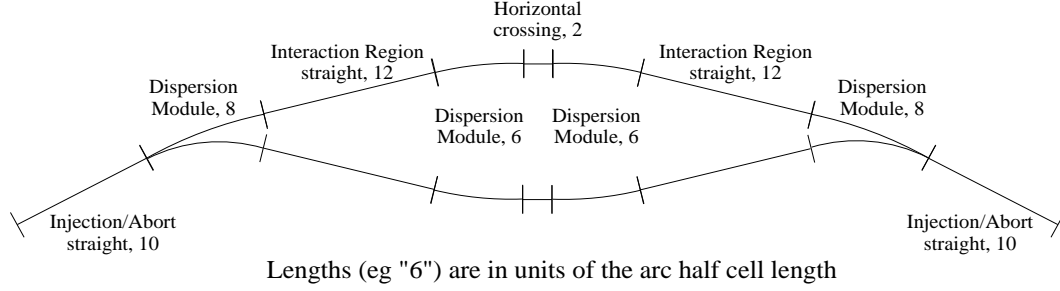


Figure 3: Cartoon of a bypass to transport low field ring beams past the experiments in Phase II operation.

Thus the half cell length is

$$L_{hc} = n_{\lambda} S_B \quad (4)$$

The bunch spacing can trivially be increased (for example during commissioning) by any of the common factors of the “half cell harmonic number”  $n_{\lambda}$ . Table 4 shows all the even values of  $n_{\lambda}$  in the half cell length range from 100 meters to 200 meters. The value of  $n_{\lambda} = 24$  was chosen for both low and high field rings in the VLHC Feasibility Study [1], corresponding to a half cell length of  $L_{hc} = 135.4865$  meters.

This half cell length is short enough to keep the natural horizontal emittance due to synchrotron radiation in the high field ring,  $\epsilon_{nat} = 0.04 \mu\text{m}$ , much smaller than the horizontal emittance  $\epsilon_x \approx 0.20 \mu\text{m}$  which must be maintained (by heating) to avoid beam-beam limits in the store. Figure 4 shows the cubic dependence of the natural emittance on the half cell length under the reasonable approximation of a purely FODO cell lattice with thin quadrupoles and 100% dipole packing fraction.

A stronger limit to the maximum arc half cell length is the need to limit the vulnerability of the low and high field rings to systematic field harmonic errors in the arc bending magnets. This is more critical for the low field ring, simply because the injection energy is an order of magnitude lower (1 TeV) than for the high field ring (10 TeV). A crude calculation [8] shows that the systematic harmonic  $b_n$  must obey

$$\frac{b_n}{r_0^n} \leq \widehat{\Delta Q_x} \frac{1}{D_n} L_{hc}^{-(n+1)/2} \left( \frac{\beta\gamma}{m^2 \epsilon_x} \right)^{(n-1)/2} \quad (5)$$

where  $r_0 = 10$  mm is the reference radius,  $\widehat{\Delta Q_x}$  is the maximum allowed tune shift,  $D_n$  is a numerical coefficient (see Table 5), and  $m$  is both the horizontal betatron amplitude in units of  $\sigma_x$  and the constant momentum offset in units of  $\sigma_p/p$ . Equation 5 assumes fully packed FODO cells with thin quads, and assumes that the betatron beam size at an F quad is equal to the momentum spread size [8]. Although crude, Eqn. 5 correctly shows the scaling with respect to injection energy and cell length. Tracking studies are necessary when increased accuracy is required.

$n_{\lambda}$	$L_{hc}$ [m]	COMMON FACTORS	
18	101.6149	2*3*3	2 3 6 9 18
20	112.9054	2*2*5	2 4 5 10 20
22	124.1959	2*11	2 11 22
<b>24</b>	<b>135.4865</b>	<b>2*2*2*3</b>	<b>2 3 4 6 8 12 24</b>
26	146.7770	2*13	2 13 26
28	158.0676	2*2*7	2 4 7 14 28
30	169.3581	2*3*5	2 3 5 6 10 15 30
32	180.6486	2*2*2*2*2	2 4 8 16 32
34	191.9392	2*17	2 17 34

Table 4: Potential arc half cell harmonics and lengths. The bunch spacing can trivially be increased by any of the common factors of the “half cell harmonic factor”,  $n_{\lambda}$ .

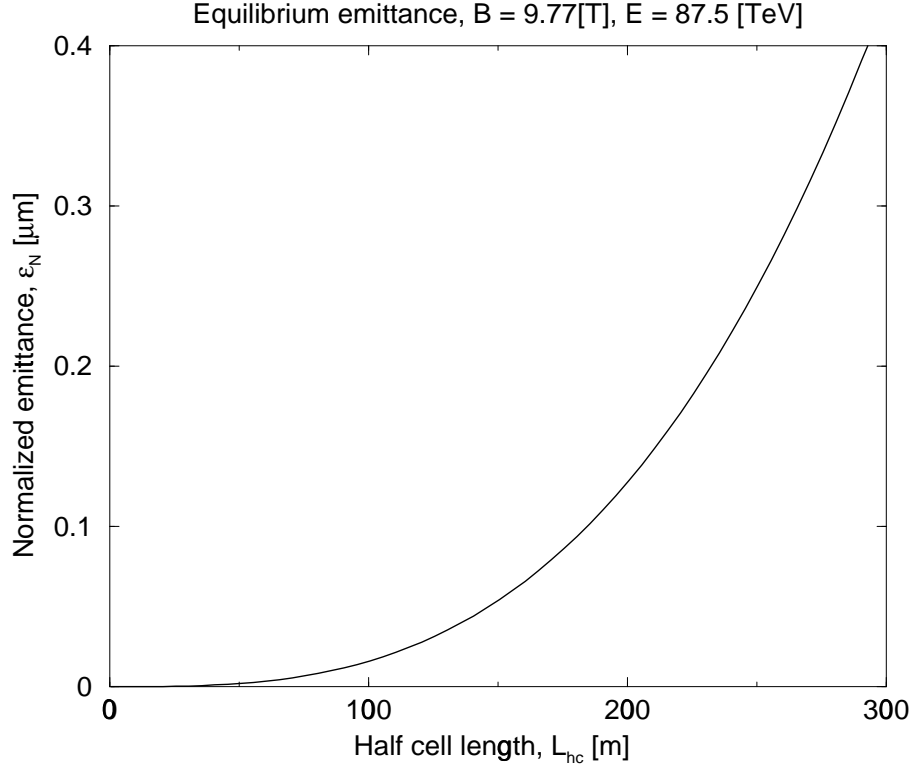


Figure 4: Natural emittance from synchrotron radiation versus arc half cell length in the high field ring.

Figure 5 illustrates how the sensitivity to systematic harmonics depends on the half cell length according to Eqn. 5, in the low and high field rings respectively.

In conclusion, the current value of  $L_{hc} = 135.4865$  m is by no means fully optimized, not least because we do not accurately understand what values of systematic magnet harmonics might be achieved in industrial production of the arc bending magnets.

n	Multipole	$D_n$
1	Quadrupole	.8333
2	Sextupole	2.412
3	Octupole	6.712
4	Decapole	19.18
5	12-pole	56.49
6	14-pole	170.9

Table 5: Lowest order  $D_n$  values, with a phase advance of  $\phi_c = 90$  degrees per FODO cell.

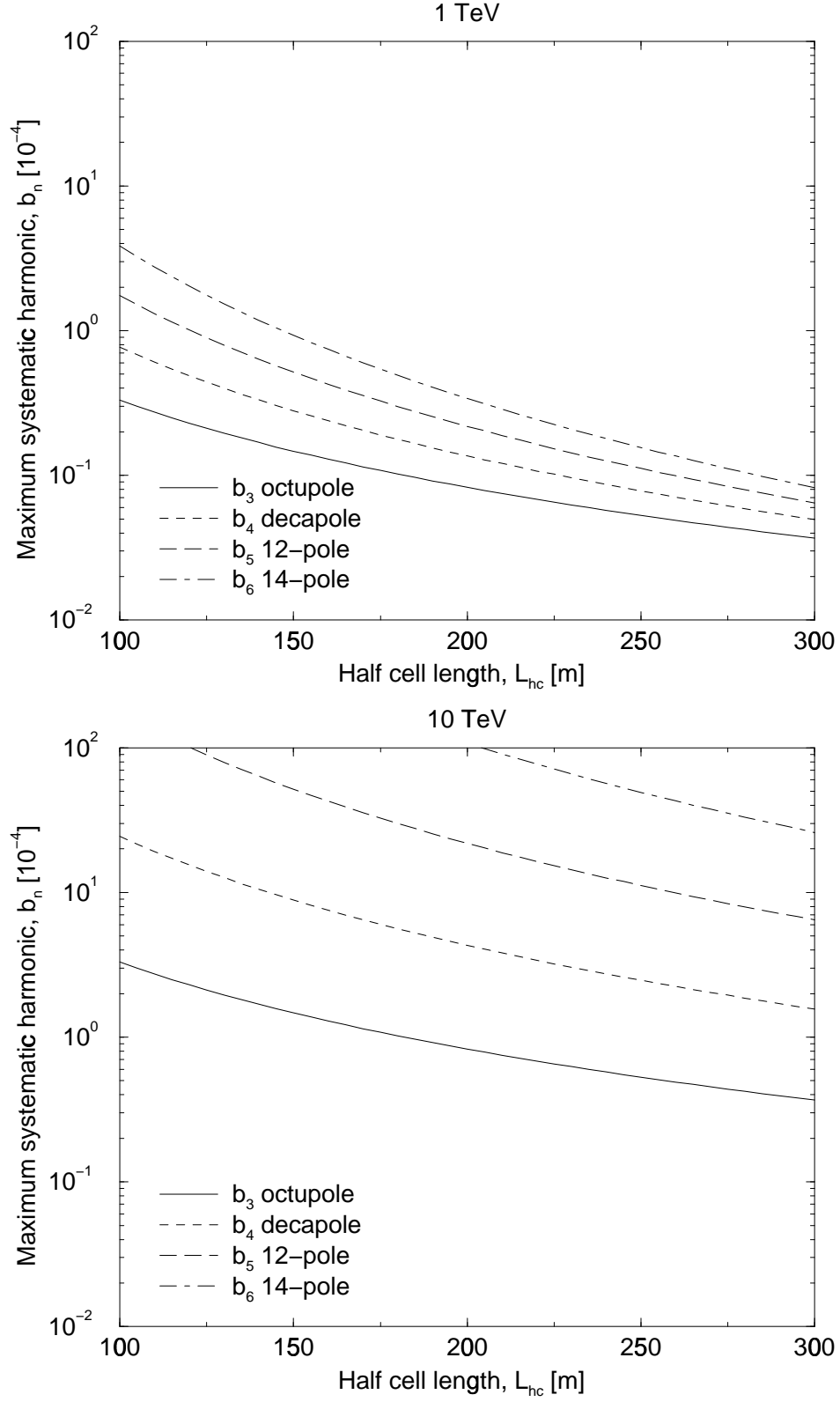


Figure 5: Maximum allowed systematic harmonics for the low field ring (top) and the high field ring (bottom) at injection energies 1 TeV and 10 TeV, versus half cell length. A maximum tune shift of  $\Delta Q = 0.05$  is permitted with an emittance of  $\epsilon = 1.5$  [ $\mu\text{m}$ ], a betatron amplitude of  $4\sigma$ , and a constant momentum offset of  $\Delta p/p = \pm 4\sigma_p/p$ .

## 2 PHASE I: THE LOW-FIELD RING (Syphers)

### 2.1 Lattice (Johnstone)

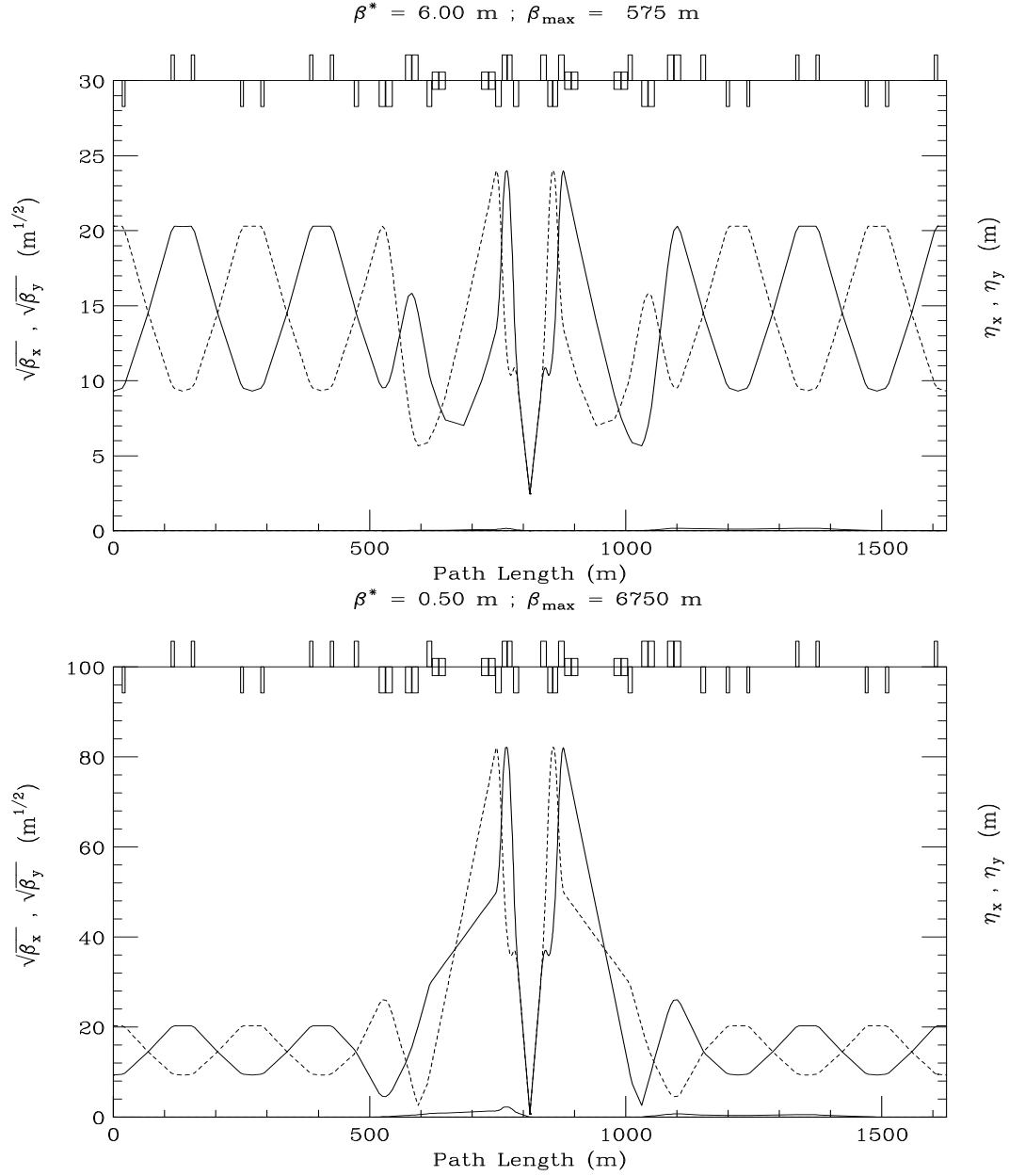


Figure 6: Variation of the IR lattice functions from the injection configuration (a) Top: through to collision (b) Bottom: During the squeeze the phase advance across the insert is fixed at  $\mu = 2.250$ .

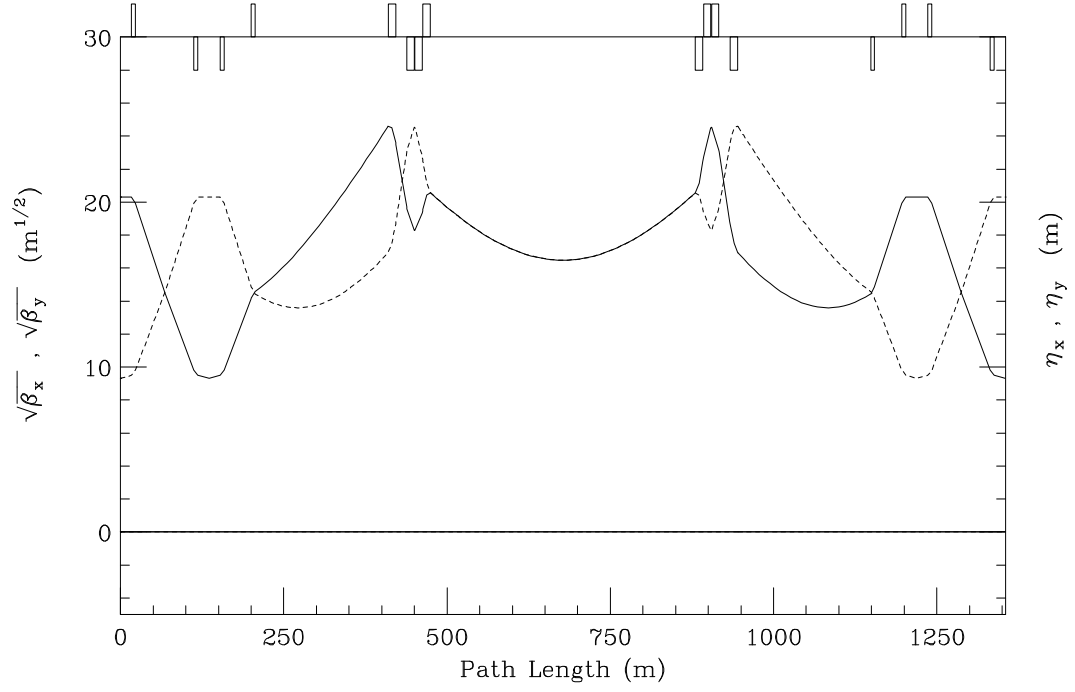


Figure 7: Layout of the IA straight supporting beam transfer from the Tevatron and VLHC abort.

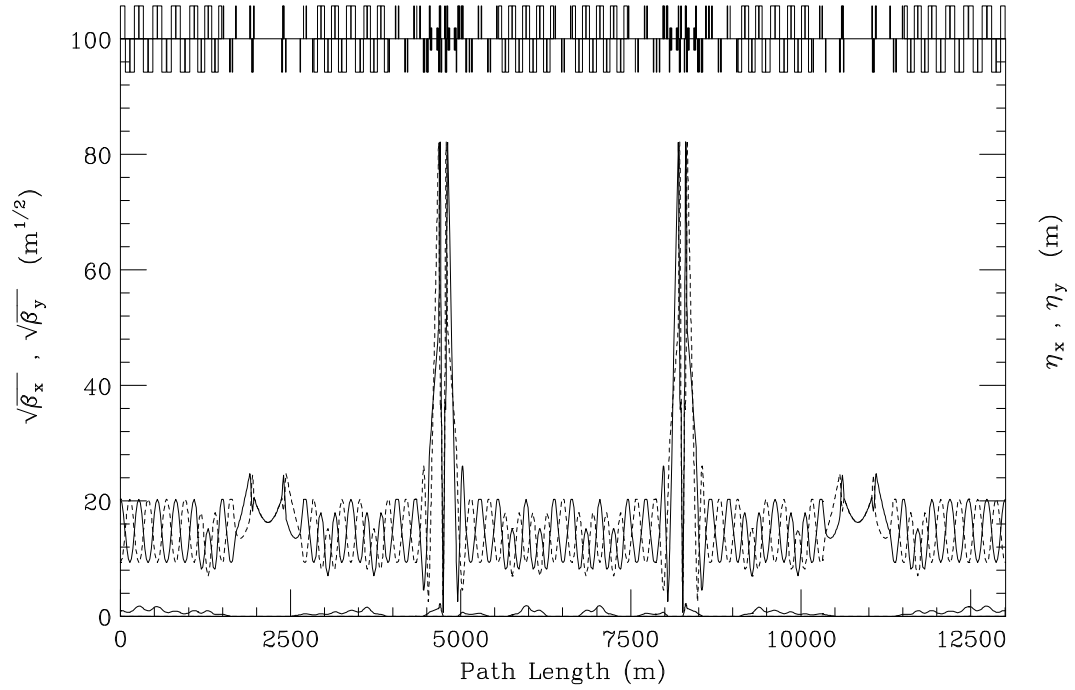


Figure 8: Lattice functions during collisions through the section of the ring containing the IR's, utility straights, and a single cell (center) where the beams cross between the inner and outer apertures.

## 2.2 Magnet aperture and field quality (Sen)

The required dynamic aperture is determined by the available mechanical aperture. Collimators define the limiting aperture in most cases and they are usually placed at around  $6\sigma$  from the center of the beam pipe. This allows for  $3\sigma$  for the beam distribution and the rest due to injection errors and orbit drifts over time. The real dynamic aperture therefore must be greater than  $6\sigma$  in order to avoid significant losses of particles at places in the ring outside the beam cleaning section.

Errors, time dependent fields and other imperfections in a real machine can never be modeled accurately enough in a simulation so the dynamic aperture calculated by a simulation always exceeds the measured dynamic aperture. Observations at HERA and SPS have shown that the agreement between the measured and calculated dynamic aperture varies between 20-100%. As a consequence the LHC, for example, requires that the calculated dynamic aperture after  $10^5$  turns at both injection and collision (with only magnetic nonlinearities) equal  $12\sigma$ . It is useful to consider the sources of discrepancies between the model and the accelerator, listed for example by Koutchouk [2].

Source or Uncertainty	Impact	D.A in $\sigma$
Target D.A after $10^5$ turns		12.0
Finite mesh size	-5%	
Linear imperfections	-5%	
Amplitude ratio $x_i/y_i$	-5%	
Extrapolation to $4 \times 10^7$ turns	-7%	9.6
Time-dependent multipoles	-10%	
Ripple	-10%	
Safety margin	-20%	
Long-term DA		6.2

Table 6: Sources of uncertainties in the numerical calculation of dynamic aperture, taken from [2].

The linear imperfections include orbit errors due to misalignments and gradient errors and the loss of 5% is assigned after correction of these errors. Since the errors listed above are just as likely for the VLHC, it seems reasonable to adopt a dynamic aperture requirement of  $12\sigma$  after  $10^5$  turns.

Non-linearity	Injection	Collision
Chromaticity sextupoles	28	$\approx 70$
Multipoles in dipoles	6.5	$> 27$
Multipoles in lattice quads	$\approx 12$	$> 27$
Multipoles in low- $\beta$ quads	$> 23$	6.5
Long-range beam-beam kicks	6.5	6

Table 7: The dynamic aperture in units of rms size  $\sigma$  due to various nonlinearities in the LHC, taken from [2].

The DA in the LHC at injection is dominated by systematic multipoles in the dipoles. The allowed harmonics - sextupole and decapole are corrected by small correction coils at the end of each dipole.

### 2.2.1 Scaling the Main Injector errors

The field harmonics in the low-field magnets will be measured in the summer of fall of 2001. As a starting hypothesis Bill Foster has proposed that the errors in the Main Injectors be used as a basis, assuming that the mechanical errors scale with the pole tip gap. Thus we assume that the field errors in the VLHC low field transmission line magnets at a pole tip radius of 1 cm are the same as the errors in the Main Injector magnets at a pole tip radius of 1 inch.

The expansion for the field error in a dipole magnet can be written in terms of coefficients  $(b_n, a_n)$  as

$$\Delta[B_y + iB_x](r, \theta) = B_0 \sum_{n=1} (b_n + ia_n) \left(\frac{r}{R_{ref}}\right)^n e^{in\theta} \quad (6)$$

at a radius  $r$  and azimuth  $\theta$ . Here  $B_0$  is the main dipole field and  $R_{ref}$  is the reference radius. Our assumption is that at every azimuth  $\theta$

$$\Delta[B_y + iB_x]^{MI}(r = 2.54\text{cm}, \theta) = \Delta[B_y + iB_x]^{VLHC}(r = 1\text{cm}, \theta) \quad (7)$$

We make the somewhat stronger assumption that the equality is satisfied for every harmonic  $n$  so that we obtain the following scaling relation between the multipole coefficients in the Main Injector and those in the VLHC,

$$\left[ \frac{b_n}{R_{ref}^n}, \frac{a_n}{R_{ref}^n} \right]^{VLHC} = (2.54)^n \frac{B_0^{MI}}{B_0^{VLHC}} \times \left[ \frac{b_n}{R_{ref}^n}, \frac{a_n}{R_{ref}^n} \right]^{MI} \quad (8)$$

Order $n$	$\langle b_n \rangle$	$\langle a_n \rangle$	$\sigma(b_n)$	$\sigma(a_n)$
2	-0.6162	0.0000	0.6162	0.2054
3	0.0000	-0.2053	0.1532	0.3080
4	0.3081	0.0000	0.3081	0.1541
5	0.0000	-0.3081	0.1026	0.5135
6	0.0000	0.0000	0.2568	0.2568

Table 8: Systematic  $\langle \rangle$  and random  $\sigma$  of multipole coefficients used for the VLHC, scaled from Main Injector magnets using Equation (8). The coefficients are shown in units of  $10^{-4}$ .

### 2.2.2 Dynamic aperture at injection

- Two programs (Teapot and Sixtrack) at two tunes: Tevatron and LHC injection
- Tevatron tunes
  - DA with chromaticity sextupoles
  - DA with only random errors. Which ones are dominant - turn off the sextupoles, octupoles, both.
  - DA with random and systematic errors. Which ones are dominant - turn off the sextupoles, octupoles, both.
  - Which errors are more important: systematic or random? Why?
- LHC Injection tunes - same issues as above

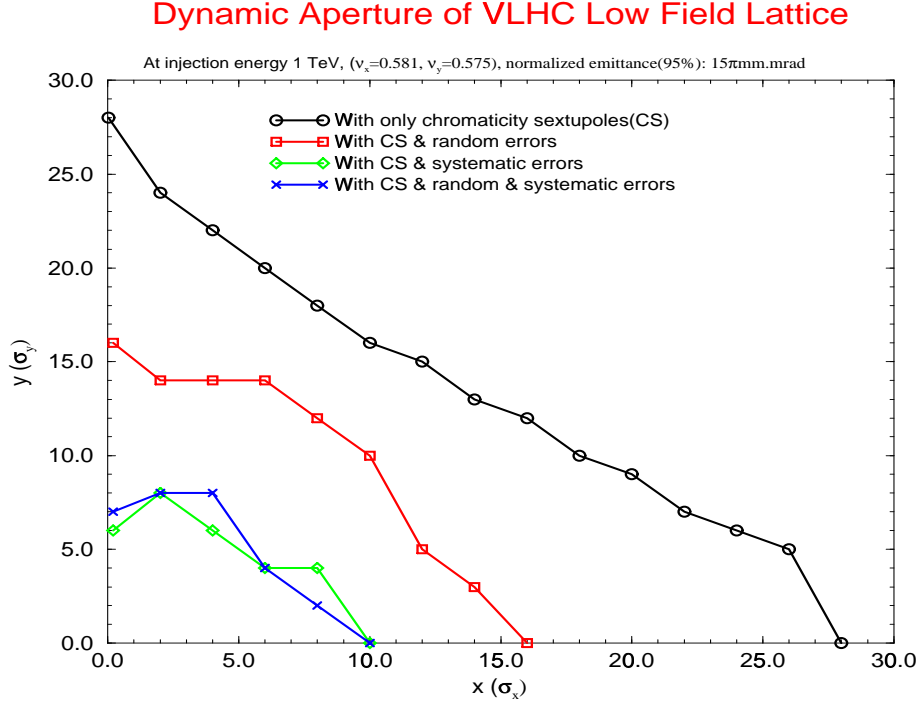


Figure 9: Dynamic aperture at injection with only chromaticity sextupoles, only random errors, only systematic and all errors. The dynamic aperture with all errors is nearly the same as that with only the systematic errors. The effects of the systematic errors therefore dominate.

Errors	Dynamic Aperture (mm)
Only chromaticity sextupoles (CS)	16.8
CS and only random errors	11.7
CS and only systematic errors	6.0
CS and all errors	6.2
CS and only random errors and $\sigma(b_2) = \sigma(a_2) = 0$	12.2
CS and only random errors and $\sigma(b_3) = \sigma(a_3) = 0$	11.0
CS and only systematic errors and $\langle b_2 \rangle = 0$	6.3
CS and only systematic errors and $\langle a_3 \rangle = 0$	7.4
CS and only systematic errors and $\langle a_3 \rangle = \langle a_5 \rangle = 0$	12.8

Table 9: Dynamic aperture at Injection energy with various sets of errors in the arc magnets. These results show that the dynamic aperture is dominated by the systematic errors, and in fact the skew systematic errors. Tune footprints show that most particles with tunes near the coupling resonance  $\nu_x - \nu_y = 0$  are lost so this suggests that correcting the coupling driven by the systematic skew multipoles might improve the dynamic aperture.

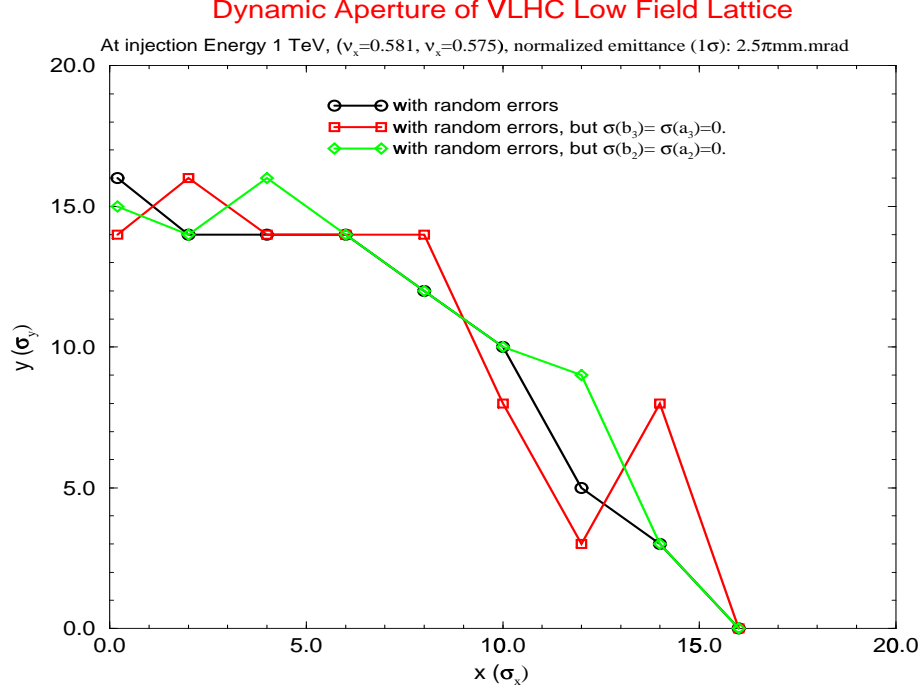


Figure 10: Dynamic aperture at injection with chromaticity sextupoles and only systematic errors. The dynamic aperture with all systematic errors is compared to that with setting the systematic  $b_2 = 0$ ,  $\langle a_3 \rangle = 0$  and both  $\langle a_3 \rangle = \langle a_5 \rangle = 0$ . The dynamic aperture is improved considerably by setting both the skew multipoles to zero. This is consistent with footprint plots which show that particles near the coupling resonance are lost.

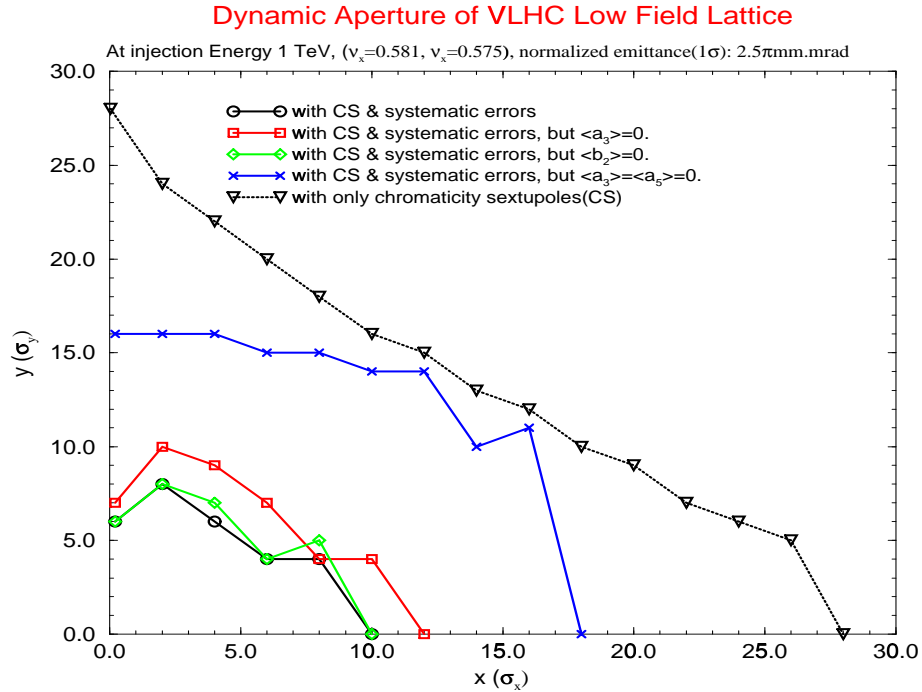


Figure 11: Dynamic aperture at injection with only random errors. The dynamic aperture with setting  $sg(b_2) = \sigma(a_2) = 0$  improves slightly compared to the case with all the random errors.

### 2.2.3 Dynamic aperture at collision

- Impact of saturation sextupole field on dynamic aperture
  - Correction with lumped and distributed sextupole correctors
- Correcting for quadrupole saturation at top energy with lumped quadrupoles
  - Any impact without misalignments, assuming phase advance per cell is corrected to  $90^\circ$  ?
  - Impact with misalignments?

The single beam dynamic aperture (DA) at collision optics will likely be dominated by the field errors of the IR quadrupoles due to the large beam sizes in these magnets. This is true for the LHC design and was also true for the SSC design. The IR quadrupoles with their high gradients will be built with “conventional” superconducting magnets. The nonlinear harmonics in these magnets are much better understood following decades of development and also the Fermilab program of building these quadrupoles for the LHC. The errors in the arc magnets built with conventional technology usually are not significant in determining the dynamic aperture at top energy. For example, the target dynamic aperture in the LHC at top energy is set at  $12\sigma$  with only the IR quadrupole field errors. We will adopt the same target DA of  $12\sigma$  in the simulations. At a location of  $\beta = 400\text{m}$ , this corresponds to a DA of  $\sim 2.5\text{ mm}$ .

The arc magnets in the phase I collider however are built with transmission line magnets which have different characteristics. At high current, the field in the iron saturates leading to a drop in the gradient and a large negative sextupole component ( $b_2$ ). While the change in gradient could be compensated by quadrupole correctors in every cell to maintain the correct phase advance per cell, the compensation of the sextupole component is a more serious issue.

The straightforward approach to compensating the saturation  $b_2$  component is to use the chromaticity sextupoles in the cells to correct the linear chromaticity. At large  $|b_2|$  this leads to strong chromaticity sextupoles lumped at two locations in the cell, one SF next to the F quadrupoles, the other SD next to the D quadrupoles. The SD sextupoles are stronger because of the smaller dispersion at their locations. A variant of this approach is to distribute the sextupoles with additional sextupoles in the 1 m gap between the F and D and the D and F quadrupoles. We place these additional two sextupoles in the same family as the SD in order to reduce their strength.

The dynamic aperture as a function of  $b_2$  for the two cases are shown in Figures 12 and 13 respectively. Figure 12 shows the DA calculated after 1024 and 10,000 turns tracking. The DA drops by less than  $2\sigma$  with the longer term tracking at all values of  $b_2$  and in many cases there is no significant change. At  $b_2 = -4 \times 10^{-4}$ , the DA drops just below the physical aperture of 9 mm compared to a DA of 19 mm at  $b_2 = 0$ . At larger  $|b_2|$  values, the DA drops more slowly, reaching 6 mm at  $b_2 = -10 \times 10^{-4}$ . If we adopt the somewhat arbitrary rule that the DA at top energy without the IR quadrupoles should exceed the physical aperture, then the maximum  $|b_2|$  allowed is about  $4 \times 10^{-4}$ . This would limit the field and the maximum energy of the collider. Figure 13 shows the DA with three SD and one SF per cell with 1024 turn tracking. For comparison, the DA with the one SD and one SF per cell is also shown. Distributing the SD sextupoles improved the DA at all values except when  $b_2 = 0$ . Compared to the first case, the DA drops below the physical aperture at the much larger value of  $|b_2| = 10 \times 10^{-4}$ . This distributed scheme of sextupoles would therefore allow an increase in the operating energy of the collider if other methods are not available.

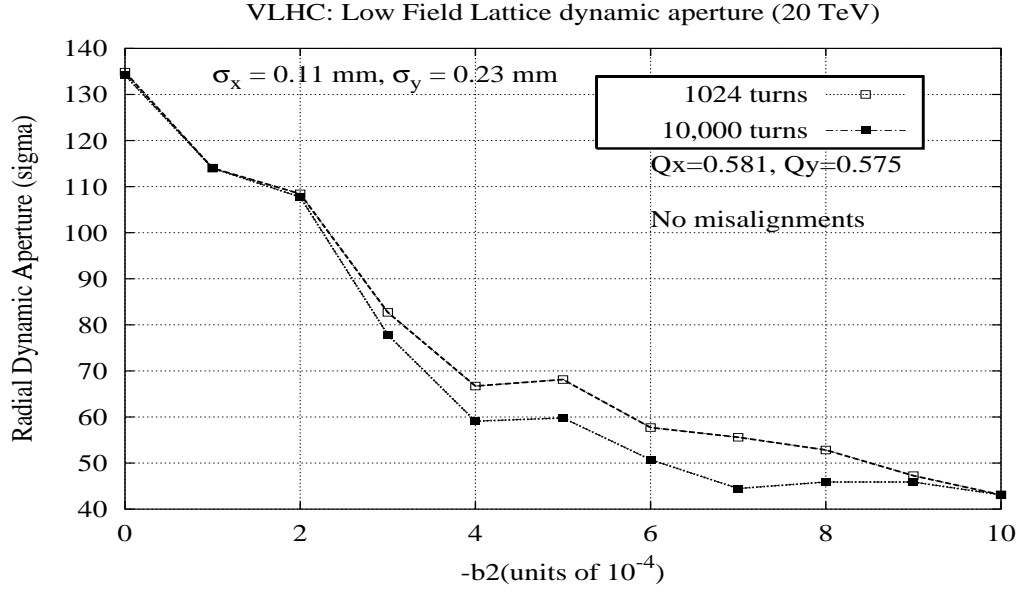


Figure 12: Dynamic aperture as a function of the saturation  $b_2$  in the arc magnets.

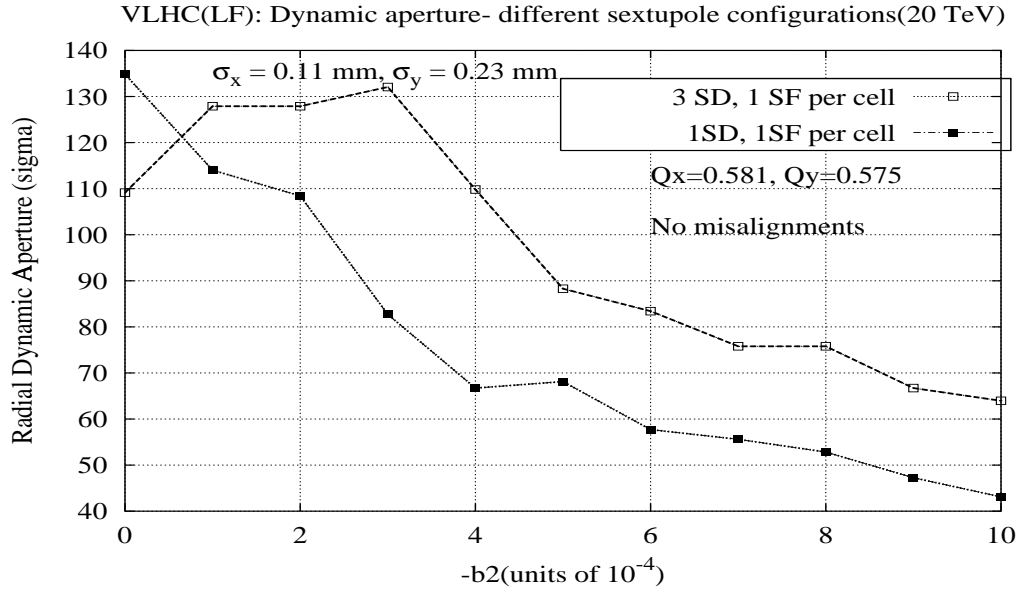


Figure 13: Dynamic aperture as a function of the saturation  $b_2$  with different sextupole configurations.

## 2.3 Tolerances (Sen)

## 2.4 Corrections

### 2.4.1 Closed orbit (Michelotti)

- Analytical estimation of closed orbit errors and comparison with error using MAD with combined function magnets.
- Closed orbit distortion with rms misalignments of 0.25mm of each 16m long section using MAD without orbit correction. Figures of closed orbit
- What are or should be the alignment requirements?
- How far apart do correctors have to be spaced?
- How strong do these correctors have to be?
- How well does the orbit have to be corrected at both injection and top energy? Beam size at  $\beta_{max}$  at injection energy is 1mm, what should be the rms closed orbit error? At top energy, beam size at same location is about 0.2mm, what should be the closed orbit error?
- Is a beam-based alignment (i.e. K-modulation) necessary? If yes, what are the requirements on instrumentation?
- Can each long magnet be equipped with steppable motors?

### 2.4.2 Other (Sen)

## 2.5 Stability issues (Ng)

The low-field VLHC has the characteristic of high particle energy, large ring circumference, and small beam pipe aperture. Some of its beam stability issues are discussed here. The first 8 rows of Table 10 are the input parameters of the collider ring for both Phase 1 and Phase 2 at injection and storage modes. The lattice of the ring is composed of regular FODO cells with  $90^\circ$  phase advance. We therefore assume the transition gamma  $\gamma_t$  to be close to the betatron tune of  $\nu_\beta \approx 270$ , from which the slip factor  $\eta$  can be computed easily.

We assume that the particle distribution inside a bunch is parabolic. Thus the half bunch length  $\hat{\ell}$  is related to the rms length  $\sigma_\ell$  by  $\hat{\ell} = \sqrt{5}\sigma_\ell$  and similarly  $\hat{\tau} = \sqrt{5}\sigma_\tau$  when expressed in terms of time.

A bunch excited by forces in the vacuum chamber oscillates in the longitudinal phase space in modes describable by the radial mode parameter  $n_r$  designating  $n_r$  radial nodes and the azimuthal mode parameter  $m$  designating  $|m|$  azimuthal nodes. For a given  $m$ , the most easily excited radial mode is  $n_r = |m|$  and only these radial modes will be included in our discussion. Almost distribution independent, the spectrum for the mode designated by  $m \neq 0$  peaks at frequency

$$f_{(m)} = \frac{|m| + 1}{2\tau_L} \quad (9)$$

where  $\tau_L$  is the *total* length of the bunch. In parabolic distribution,  $\tau_L = 2\hat{\tau} = 2\sqrt{5}\sigma_\tau$ . Actually, the spectrum of this mode is nonzero only at the  $m$ -th synchrotron sidebands of, respectively, the revolution harmonics for longitudinal discussion and the betatron tune lines for transverse discussion. For  $m = 0$ , the spectrum has a frequency spread from  $-f_{(0)}$  to  $+f_{(0)}$  with  $f_{(0)}$  given by Eq. (9). Both  $f_{(0)}$  and  $f_{(1)}$  are listed in Table 10. Note that these the frequencies for the VLHC bunch modes are in the GHz range.

### 2.5.1 Resistive wall

Here, we assume that the resistive wall impedances of the beam pipe dominate. The beam pipe is cylindrical with a radius of  $b = 9$  mm. The longitudinal impedance of the beam pipe wall is

$$\left[ \frac{Z_{\parallel}}{n} \right]_{\text{wall}} = (1 + j) \frac{R\rho}{b\delta_1} |n|^{-1/2} , \quad (10)$$

Table 10: Parameters of the VLHC ring in Phase 1 and Phase 2, at injection and storage modes. The first 8 rows are input.

	PHASE 1		PHASE 2		
	Injection	Storage	Injector	Storage	
Circumference $C = 2\pi R$	241.00	241.00	241.00	241.00	km
Energy $E$	1.0	20.0	15.0	87.5	TeV
Number per bunch $N_b$	$10.00 \cdot 10^{10}$	$5.00 \cdot 10^{10}$	$10.00 \cdot 10^{10}$	$1.38 \cdot 10^{10}$	
Rf harmonic $h$	341500	341500	683000	68300	
Betatron tune $\nu_\beta$	270	270	270	270	
Rms bunch length $\sigma_\ell$	6.30	4.80	6.30	3.30	cm
Rms energy spread $\sigma_\delta$	$5.00 \cdot 10^{-5}$	$5.00 \cdot 10^{-5}$	$5.00 \cdot 10^{-5}$	$5.00 \cdot 10^{-5}$	
Beam pipe radius $b$	9.0	9.0	9.0	9.0	mm
Synchrotron tune $\nu_s$	$4.18 \cdot 10^{-4}$	$5.48 \cdot 10^{-4}$	$4.18 \cdot 10^{-4}$	$7.97 \cdot 10^{-4}$	
Rf voltage w/o impedance $V_{\text{rf}}$	0.234	8.06	1.75	37.3	MV
Freq at bunch mode $m = 0, f_{(0)}$	0.532	0.698	0.532	1.02	GHz
Freq at bunch mode $m = \pm 1, f_{(1)}$	1.06	1.28	1.06	2.03	GHz
Mode coupling limit $(Z_{\parallel}/n)_{\text{eff}}$	0.013	0.409	0.201	4.45	$\Omega$
Mode coupling limit $(Z_{\perp})_{\text{eff}}$	1.08	43.3	16.3	687	M $\Omega$ /m
Resistivity of stainless steel $\rho = 0.74 \mu\Omega\text{-m}$					
skin depth at revolution harmonic $\delta_1 = 1.23 \text{ cm}$					
wall impedances at revolution harmonic: $Z_{\parallel} = 257(1+j) \Omega$ , $Z_{\perp} = 2.43 \cdot 10^5(1+j) \text{ M}\Omega/\text{m}$					
$\text{Re}$ or $\text{Im}(Z_{\parallel}/n)_{\text{wall}}$ at rf freq	0.440	0.440	0.311	0.311	$\Omega$
Voltage distortion	6.12	5.27	4.33	2.18	MV
$\text{Re}$ or $\text{Im}(Z_{\parallel}/n)_{\text{wall}}$ at $m = 1$	0.278	0.254	0.278	0.201	$\Omega$
$\text{Re}$ or $\text{Im}(Z_{\perp})_{\text{wall}}$ at $m = -1$	263	240	263	190	M $\Omega$ /m
Resistivity of aluminum $\rho = 0.0265 \mu\Omega\text{-m}$					
skin depth at revolution harmonic $\delta_1 = 0.232 \text{ cm}$					
wall impedances at revolution harmonic: $Z_{\parallel} = 48.6(1+j) \Omega$ , $Z_{\perp} = 4.60 \cdot 10^4(1+j) \text{ M}\Omega/\text{m}$					
$\text{Re}$ or $\text{Im}(Z_{\parallel}/n)_{\text{wall}}$ at rf freq	0.0832	0.0832	0.0588	0.0588	$\Omega$
Voltage distortion	1.16	0.998	0.819	0.412	MV
$\text{Re}$ or $\text{Im}(Z_{\parallel}/n)_{\text{wall}}$ at $m = 1$	0.0526	0.0480	0.0526	0.0380	$\Omega$
$\text{Re}$ or $\text{Im}(Z_{\perp})_{\text{wall}}$ at $m = -1$	49.8	45.5	49.8	36.0	M $\Omega$ /m

where  $\rho$  is the resistivity of the beam pipe wall and

$$\delta_1 = \frac{\sqrt{2\rho}}{\omega_0\mu} \quad (11)$$

is the skin depth at the revolution harmonic and  $\mu$  the magnetic permeability. The transverse impedance is

$$[Z_{\perp}]_{\text{wall}} = \frac{2R}{b^2} \left[ \frac{Z_{\parallel}}{n} \right]_{\text{wall}}, \quad (12)$$

with  $|n|^{-1/2}$  replaced by  $|n - \nu_\beta|^{-1/2}$ . These are computed for both a stainless steel beam pipe and an aluminum beam pipe in Table 10.

### 2.5.2 Potential-well distortion

To maintain the prescribed bunch length  $\sigma_\tau$  and energy spread  $\sigma_\delta$ , the beam particle must performs synchrotron oscillation with the synchrotron tune

$$\nu_s = \frac{|\eta|\sigma_\delta}{\omega_0\sigma_\tau} \quad (13)$$

where  $f_0 = \omega_0/(2\pi)$  is the revolution frequency. Knowing the rf harmonic, the rf voltage required  $V_{\text{rf}}$  can be computed. However, this is only the rf voltage in the absence of impedance. Both  $\nu_s$  and  $V_{\text{rf}}$  are listed in Table 10.

In the presence of an inductive impedance  $\mathcal{Im} Z_{\parallel}/n$ , the particles inside a bunch see a force proportional to the gradient of the particle distribution. At a point with a time advance  $\tau$  with respect to the synchronous particle, the beam particle sees a potential drop or voltage of

$$V_{\text{ind}} = \frac{3eN_b}{2\omega_0\hat{\tau}^2} \frac{\mathcal{Im} Z_{\parallel}}{n} \frac{\tau}{\hat{\tau}}, \quad (14)$$

which is to be added to the rf voltage supplied by the klystron. Thus, for an inductive impedance at the rf harmonic, this induce voltage enhances the supplied rf voltage. The bunch shape will be distorted and its length shortened. Take, for example, Phase 1 at injection,  $V_{\text{ind}} = 6.12$  MV at  $\tau = \hat{\tau}$ , which is very much larger than the  $V_{\text{rf}} = 0.234$  MV computed earlier when there is no impedance. Thus the bunch will be very much shortened. For protons, the bunch area is conserved, implying that the energy spread will increase, may be to a value exceeding the ring momentum aperture. For Phase 1 at storage,  $V_{\text{ind}} = 5.27$  MV is still large compare with 8.06 MV computed without impedance. We find that the inductive force is still too large for Phase 2 at injection but is small enough at storage. When an aluminum beam pipe is used, where the resistivity  $\rho$  is smaller by 28 times, the potential-well distortion due to the inductive wall becomes negligible for Phase 1, but it is still too big for Phase 2 at injection.

### 2.5.3 Longitudinal mode-coupling instability

For only motion in the longitudinal phase space, mode  $m = 0$  represents static motion like potential-well distortion that we discussed before. The next modes are the dipole mode  $m = 1$  and quadrupole mode  $m = 2$ . In the presence of coupling impedance, the synchrotron sidebands are no longer equally separated with the  $m$ -th sideband at  $\pm m\nu_s f_0$ . The  $m = 2$  sideband will move towards the  $m = 1$  sideband as coupling impedance and/or bunch intensity increase. When the two sidebands merge into one, or the  $m = 1$  and  $m = 2$  modes couple, an instability will develop. The threshold is given by, for parabolic distribution,

$$\left[ \frac{\mathcal{Im} Z_{\parallel}}{n} \right]_{\text{eff}} \leq \frac{|\eta|E}{eI_{\text{pk}}} \left[ \frac{\Delta E}{E} \right]_{\text{FWHM}} \quad (15)$$

where  $I_{\text{pk}} = 3eN_b/(4\hat{\tau})$  is the bunch peak current, and the effective impedance is

$$\left[ \frac{\mathcal{Im} Z_{\parallel}}{n} \right]_{\text{eff}} = \frac{\int d\omega \frac{\mathcal{Im} Z_{\parallel}}{\omega} \omega_0 h_m(\omega)}{\int d\omega h_m(\omega)}, \quad (16)$$

and  $h_m(\omega)$  the power spectrum of mode  $m$  and  $\int d\omega$  implies discrete summation over the  $m$ -th synchrotron sideband. The longitudinal mode-coupling stability limits are listed in Table 10 for various situations of operation. The instability first develops near  $m = 1$ . Thus we evaluate the resistive wall impedance at  $f_{(1)}$ , with results shown in Table 10. We see that with a stainless steel beam pipe, instability will develop in Phase 1 at injection and become stable at storage. For Phase 2, injection can be slightly unstable but the storage mode is stable. With an aluminum beam pipe instability will develop only in Phase 1 at injection. This instability is not death threatening, stability will be regained after the bunch is lengthened and the energy spread increases

### 2.5.4 Transverse mode-coupling instability

With transverse motion, the  $m = 0$  is a valid mode, which describes the bunch making rigid dipole oscillation in the transverse plane. This corresponds to just the pure betatron sidebands. Driven by the transverse impedance, the betatron tune decreases and the pure betatron sideband moves towards its first lower synchrotron  $m = -1$  sideband. An instability will develop when the two overlap, which we call transverse mode-coupling instability. For an average bunch current  $I_b$ , the threshold driving impedance is

$$[\mathcal{Im} Z_{\perp}]_{\text{eff}} \leq \frac{2E\omega_0^2 \nu_{\beta} \nu_s \tau_L}{eI_b c}, \quad (17)$$

where the effective transverse impedance is

$$[\mathcal{Im} Z_{\perp}]_{\text{eff}} = \frac{\int d\omega \mathcal{Im} Z_{\perp}(\omega) h_m(\omega)}{\int d\omega h_m(\omega)}, \quad (18)$$

and  $\int d\omega$  implies discrete summation over the  $m = -1$  synchrotron sidebands of the betatron tune lines. These limits for various operations are listed in Table 10. Since the two modes couple near  $m = 0$ , the resistive wall impedance is evaluated at frequency  $f_{(0)}$ . The results as seen in Table 10 shows that the impedance exceeds the stability limit by very much except for Phase 2 at storage, when stainless steel is used. With an aluminum beam pipe, the storage mode of Phase 1 becomes barely stable. However, the two phases are still unstable at injection. Transverse mode-coupling instability is devastating. The growth time is usually small.

#### **2.5.5 Other issues**

We have not studied all types of instability. There are many bunches in the collider ring. Therefore, coupled-bunch instabilities in both the longitudinal and transverse planes can be serious, and an investigation is required. The beam pipe has a small bore. As a result, the image contribution to the coherent and incoherent betatron tune shifts can be important.

For the mode-coupling instabilities that we discussed above, only estimates were used to compute the thresholds. More numerical computation is necessary.

Also one should have a more thorough study of the impedance budget of the collider ring, and see whether contribution from sources other than resistive wall is important or not.

## **2.6 Polarization discussion (Vogt)**

## **2.7 Beam transfer from low field to high field (Gelfand)**

### 3 PHASE II: THE HIGH-FIELD RING

#### 3.1 Operational scenarios (Peggs)

The instantaneous luminosity is

$$L = \frac{M}{4\pi T} \frac{N^2}{\sigma_x^* \sigma_y^*} \quad (19)$$

$$= \frac{M}{4\pi T} \frac{N^2 \gamma}{\sqrt{\epsilon_x \epsilon_y \beta_x^* \beta_y^*}} \quad (20)$$

where  $T$  is the revolution period, and the flatness of the beam is conveniently measured by

$$\kappa = \frac{\epsilon_y}{\epsilon_x} \quad (21)$$

Figure 4 shows how the natural horizontal emittance varies with the arc half cell length, with a nominal value of  $\epsilon_{nat} = 0.04 \mu\text{m}$ . If the linear coupling and the vertical dispersion in the arcs are both well controlled, and in the absence of stray sources of diffusion or deliberate beam heating, the horizontal emittance will decrease to this value. The equilibrium vertical emittance can become much smaller – the beams can become very flat. There is no reason why the high field ring should not be able to achieve  $\kappa \approx 0.1$  or less, in common with conventional electron storage rings.

Storage energy, $E$	87.5	TeV
Peak luminosity, $L_{max}$	$2 \times 10^{34}$	$\text{cm}^{-2}\text{s}^{-1}$
Total cross section at store	$1.5 \times 10^{-25}$	$\text{cm}^2$
Collision debris power, per IP	84	kW
Dipole field at storage	9.765	T
Number of interaction points	2	
Distance from IP to first magnet	30	m
Injection energy	10	TeV
Fill time	30	s
Acceleration time	2000	s
Transverse emittance, rms (inject)	1.5	$\mu\text{m}$
Longitudinal emittance, rms (inject)	2.0	eV-s
Bunch spacing (53.1 MHz)	5.645	m
	18.8	ns
Initial bunch intensity, $N$	$9 \times 10^9$	
Number of buckets,	41280	
Number of bunches, $M$	37152	
Fraction of buckets filled	90	%
Protons per beam	3.34	$10^{14}$
Beam current	68.9	mA
Collision beta horz, $\beta_x^*$	3.7	m
Collision beta vert, $\beta_y^*$	0.37	m
Natural transverse emittance (H)	.0397	$\mu\text{m}$
Equilibrium emittance (H) $\epsilon_x$	$\sim 0.20$	$\mu\text{m}$
Equilibrium emittance (V) $\epsilon_x$	$\sim 0.02$	$\mu\text{m}$
Equilibrium emittance ratio, $\kappa$	0.1	
Natural RMS momentum width	$5.5 \times 10^{-6}$	

Table 11: Nominal parameters for stores in the high field ring.

INJECTION		
Emittance, rms (H and V)	1.5	$\mu\text{m}$
Momentum width, rms	233.1	$10^{-6}$
Arc bunch size (betatron)	751	$\mu\text{m}$
Arc bunch size (dispersion)	330	$\mu\text{m}$
RF voltage	50.0	MV
Longitudinal rms emittance	2.0	eV-s
Longitudinal beta	351	m
Bunch length, rms	81.9	mm
Synchrotron tune	.00280	
Synchrotron frequency	3.60	Hz
STORE BEGINNING		
Emittance, rms (H and V)	1.5	$\mu\text{m}$
Momentum width, rms	64.8	$10^{-6}$
Arc bunch size (betatron)	254	$\mu\text{m}$
Arc bunch size (dispersion)	92.0	$\mu\text{m}$
Full crossing angle	65.9	$\mu\text{rad}$
RF voltage	200	MV
Longitudinal rms emittance	2.0	eV-s
Longitudinal beta	520	m
Bunch length, rms	33.7	mm
Synchrotron tune	.00189	
Synchrotron frequency	2.44	Hz
EARLY PLATEAU (Flat beams)		
Beam-beam parameter	.008	
Emittance, rms (H)	.20	$\mu\text{m}$
Emittance, rms (V)	.02	$\mu\text{m}$
Momentum width, rms	50.0	$10^{-6}$
Arc bunch size (betatron)	32.2	$\mu\text{m}$
Arc bunch size (dispersion)	71.0	$\mu\text{m}$
IP bunch size (H)	2.89	$\mu\text{m}$
IP bunch size (V)	.29	$\mu\text{m}$
Full crossing angle	6.5	$\mu\text{rad}$
RF voltage	200	MV
Longitudinal rms emittance	1.191	eV-s
Longitudinal beta	520	m
Bunch length, rms	26.0	mm
Synchrotron tune	.00189	
Synchrotron frequency	2.44	Hz

Table 12: Store parameters, including longitudinal and RF.

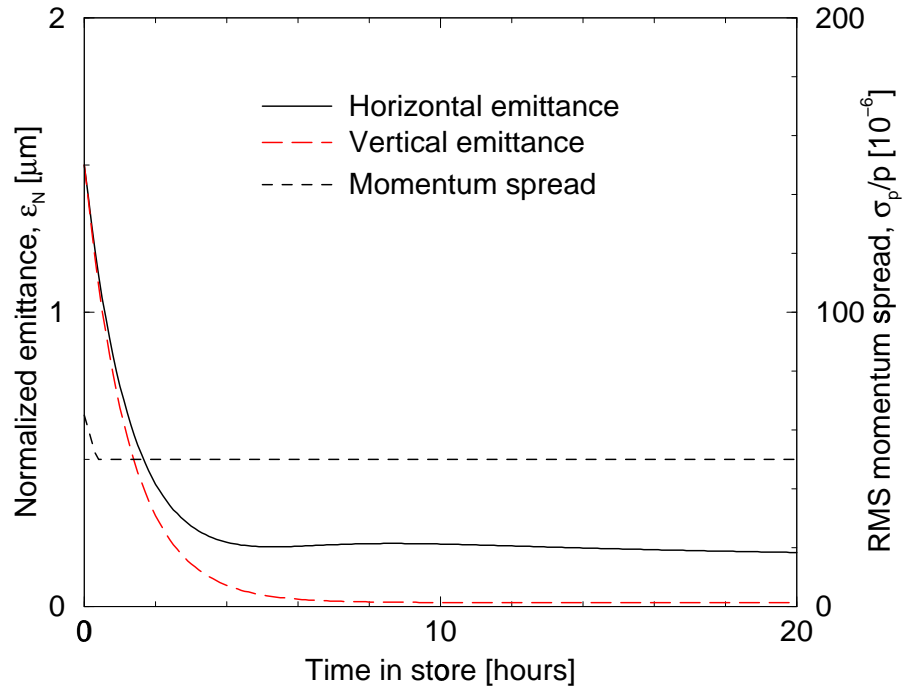


Figure 14: Evolution of the transverse emittance and the rms momentum spread during a store.

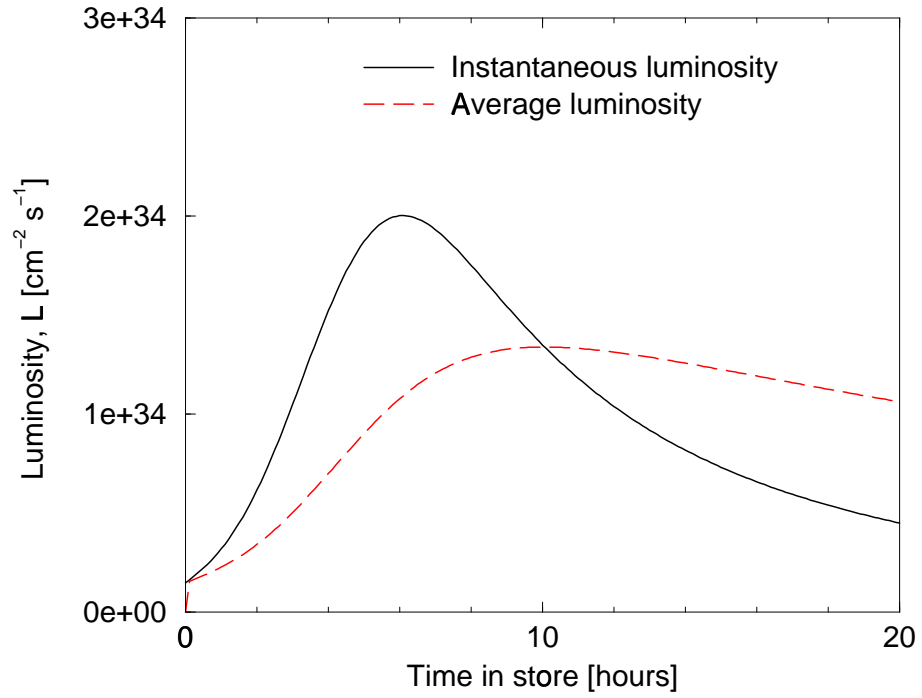


Figure 15: Evolution of the instantaneous and average luminosities, during a store.

The total number of protons in the ring,  $MN$ , is approximately set by the need to provide enough for “luminosity burn-off”, plus an overhead fraction that is dumped at the end of the store. Since the number of bunches  $M$  is fixed (with a bunch spacing of 18.8 ns), then the need for a peak luminosity of  $2 \times 10^{34} \text{cm}^{-2} \text{s}^{-1}$  sets the single bunch population to be about  $N = 9 \times 10^9$ . It is the head on beam-beam interaction which sets the minimum horizontal emittance, whether the beams are flat or round. Consistent with the beam-beam limit, Figure 14 shows the horizontal and vertical emittances decreasing to plateau values of  $\epsilon_x \approx 0.20 \mu\text{m}$  and  $\epsilon_y \approx 0.02 \mu\text{m}$ , for the nominal parameters in Table 11. Store evolution parameters, including RF and longitudinal, are summarized in Table 12. Figure 15 shows the corresponding evolution of instantaneous luminosity, and its average, during the store.

It is shown immediately below that, at the beam-beam limit, flat beams permit the product  $\epsilon_x \epsilon_y$  to be greatly reduced, relative to round beams. Equation 20 shows that this then permits larger values for  $\beta_x^*$  and  $\beta_y^*$  at fixed luminosity. Flat beams permit more relaxed IR optics, even before the increased efficiencies of doublet optics are considered.

### 3.1.1 The head on beam-beam interaction

The horizontal and vertical tune shift parameters for bi-gaussian beams are

$$\xi_{x,y} = \frac{r}{2\pi\gamma} \frac{N\beta_{x,y}^*}{\sigma_{x,y}^* (\sigma_x^* + \sigma_y^*)} \quad (22)$$

where  $r = 1.535 \times 10^{-18} \text{m}$  is the classical radius of the proton. When the beams are round ( $\beta_x^* = \beta_y^*$ ,  $\epsilon_x^* = \epsilon_y^*$ ) this reduces to

$$\xi_x = \xi_y = \frac{r}{4\pi} \frac{N}{\epsilon_x} \quad (23)$$

with no dependence on  $\gamma$  or  $\beta^*$ . By comparison, if the beams are very flat,  $\kappa \ll 1$ , then

$$\xi_x = \xi_y = \frac{r}{2\pi} \frac{N}{\epsilon_x} \quad (24)$$

The horizontal and vertical beam-beam parameters are made equal here by asserting that the  $\beta^*$  ratio is also  $\kappa$

$$\kappa = \frac{\epsilon_y}{\epsilon_x} = \frac{\beta_y^*}{\beta_x^*} = \frac{\sigma_y^*}{\sigma_x^*} \quad (25)$$

Equations 23 and 24 show that, whether the beam is round or flat, the beam-beam parameter depends only (directly) on the horizontal emittance  $\epsilon_x$ .

The beam-beam limit is expected to be (approximately) the same for round or flat beams, given by

$$\xi \leq 0.008 \quad (26)$$

The numerical value of 0.008 is illustrated in Figure 16, which displays empirical data compiled by Keil and Talman for electron storage rings [25]. Equations 23 and 24 show that the minimum value of  $\epsilon_x$  permitted by the beam-beam effect is the same for flat or round beams, within about a factor of 2. Then, re-writing Eqn. 20 as

$$L = \frac{M}{4\pi T} \frac{N^2 \gamma}{\kappa \epsilon_x \beta_x^*} \quad (27)$$

it is explicitly clear that the value of  $\beta_x^*$  can be increased by a factor of about  $1/\kappa$ , a large amount and a significant advantage. The value of  $\beta_y^*$  is about the same for flat or round beams. Figure 17 shows how the horizontal and vertical beam-beam parameters evolve during the store. Approximately 70% of the original beam is burned off after 20 hours.

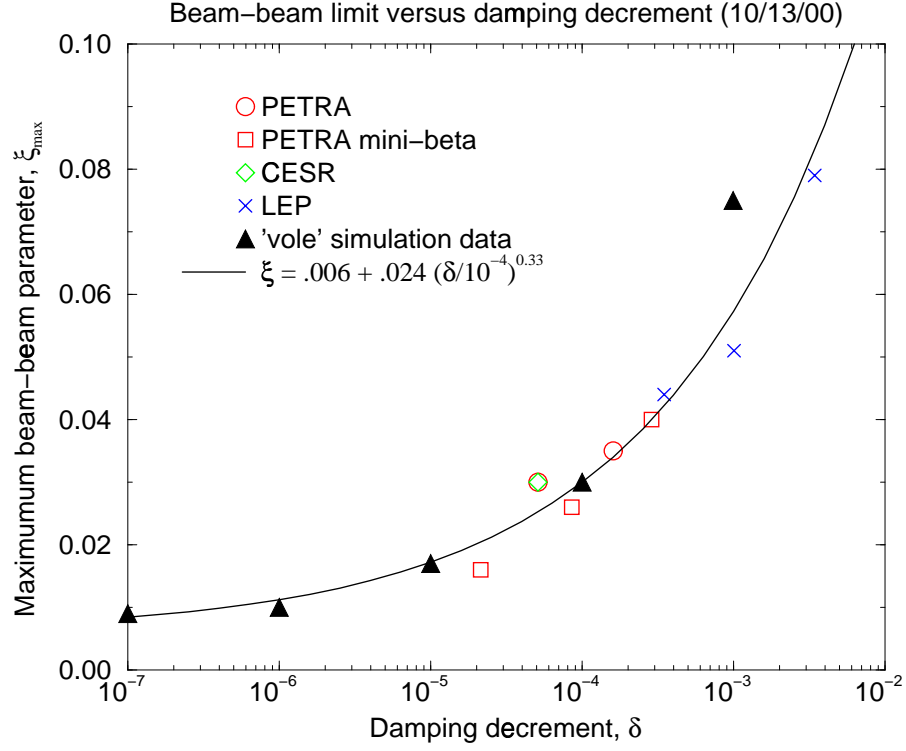


Figure 16: The beam-beam limit versus damping decrement in electron colliders, extrapolated by tracking towards VLHC parameters.

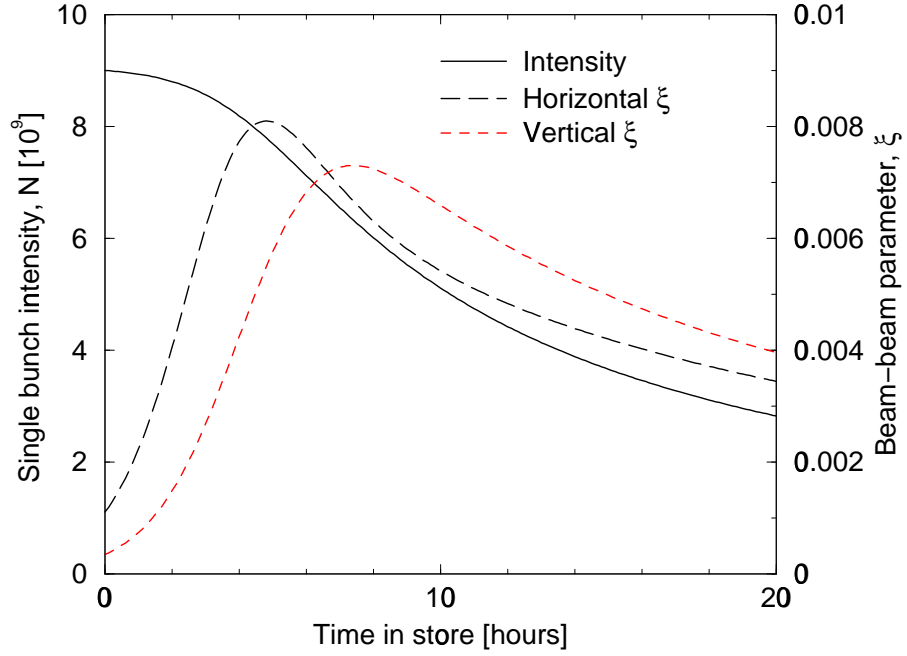


Figure 17: Evolution of beam-beam parameters, and the single bunch intensity, during the store.

### 3.1.2 Crossing angles and parasitic beam-beam collisions.

Since the collision beta functions  $\beta_x^*$  and  $\beta_y^*$  do not influence the beam-beam parameters, they are adjusted (with a fixed ratio  $\kappa$ , and for given values of  $M, N$ , and  $\epsilon_x$ ) in order to achieve the required peak luminosity.

Most (or many) of the parasitic collisions occur in the drift region next to the IP, where the beta functions at a distance  $s$  from the IP are given by

$$\beta = \beta^* + \frac{s^2}{\beta^*} \quad (28)$$

When  $s \gg \beta^*$  – except for the first parasitic collision – the horizontal beta function is much less than the horizontal

$$\frac{\beta_x}{\beta_y} \approx \kappa \quad (29)$$

The total horizontal and vertical tune shifts due to all parasitic collisions around a single IP are given by

$$\Delta Q_{x,y} = \pm \frac{rN}{2\pi\gamma} \left\langle \frac{\beta_{x,y}}{\Delta^2} \right\rangle \frac{4L_{sep}}{S_B} \quad (30)$$

where  $\Delta$  is the full vertical beam separation,  $S_B$  is the longitudinal bunch separation, and angle brackets  $\langle \rangle$  indicate an average over the parasitic collision region, within  $\pm L_{sep}$  of the IP. The tune shift is positive in the same plane as the separation.

Taken together, Eqns, 29 and 30 show that a further advantage of flat beams is that the horizontal long range tune shift is much smaller than the vertical, and much smaller than it would be with round beams,

$$\Delta Q_x \simeq -\kappa \Delta Q_y \quad (31)$$

This is illustrated in Figure 18, where the total vertical crossing angle  $\alpha$  evolves in order to keep the beams approximately  $n = 10$  of vertical beam sigmas apart

$$\Delta = \alpha s = n\sigma_y^* s \approx n\sigma \quad (32)$$

Equation 30 shows that, if the beam separation plane is changed from vertical to horizontal with the total crossing angle  $\alpha$  held fixed, then the long range tune shifts change sign with almost unchanged absolute values. In the drift region the horizontal and vertical angular divergences of the beam are equal, even for flat beams, since

$$\frac{\sigma_y'^*}{\sigma_x'^*} = \sqrt{\frac{\epsilon_x \beta_x^*}{\epsilon_y \beta_y^*}} = \sqrt{\frac{\kappa}{\kappa}} = 1 \quad (33)$$

For parasitic collisions (except the first) the beams are essentially round, even with flat beams at the IP!

If the separation plane at one IP is vertical, and at the other horizontal, then significant tune shift cancellations can be achieved. However, the beams are vertically separated in the arcs, no matter what the local crossing plane, because of the use of common coil magnet technology in the arc cells. Conversion from a horizontal beam separation plane to vertical separation in the arcs is not expected to be fundamentally difficult, even though the optical design of such a scheme has not yet been addressed.

All electron colliders take advantage of the fact that flat beams allow the use of quadrupole doublets in the interaction region, with significant advantages over the triplet solutions which traditionally are necessary with round beams in hadron colliders. Because the “center of gravity” of a doublet is closer to the IP than an equivalent triplet, then the maximum beta values  $\hat{\beta}$  with doublet optics are less than those with triplet optics – assuming the distance to the nearest quadrupole from the IP is held fixed [24]. The contribution of a doublet to the natural chromaticity in collision optics is also systematically less than with triplet optics [24]. This can be understood heuristically by considering the presence of the first quad in a triplet to be necessary merely to split the horizontal and vertical beta functions, in order for the following two quads to act as a doublet. If the initial beta functions are already well separated – with flat beams – there is no need for the “beta splitting” first quadrupole.

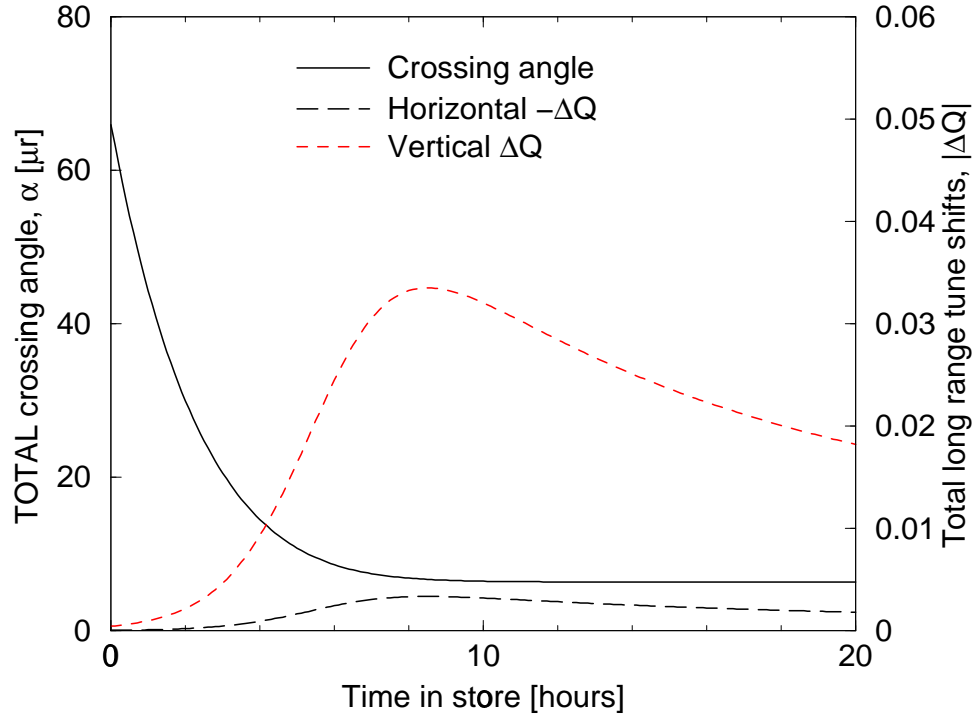


Figure 18: Evolution of the long range tune shifts, and the vertical crossing angle, during the store.

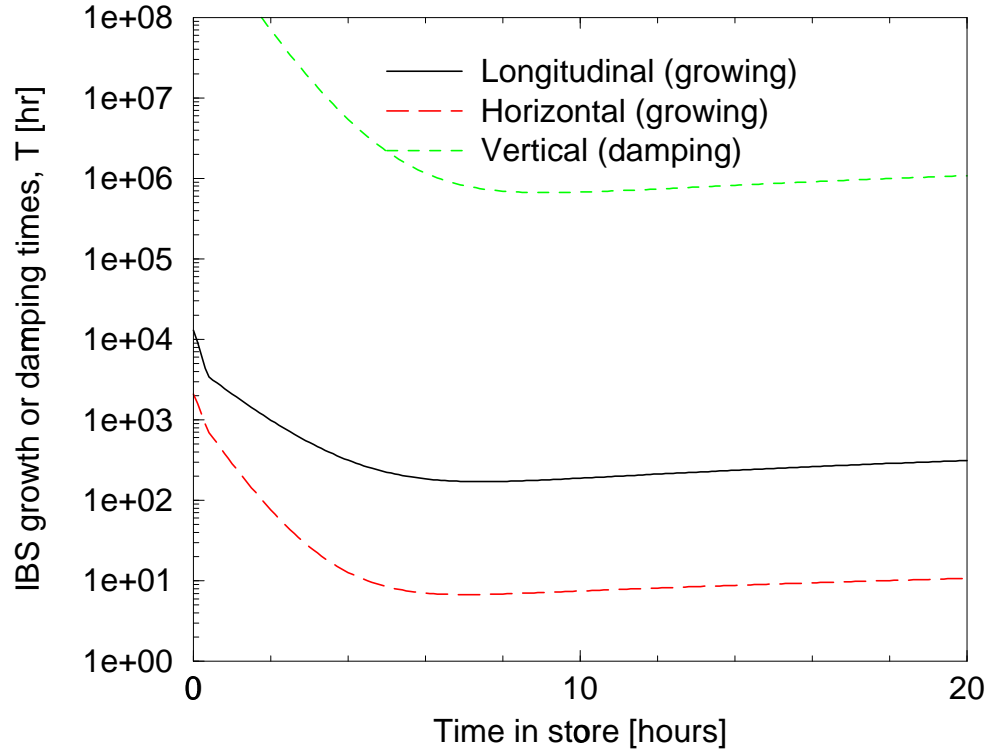


Figure 19: Intra beam scattering growth (or damping) times during the store.

Flat beams require the first quadrupole on both sides of the IP to be vertically focusing. Thus, the optics must be symmetric across the IP, and the beams must be separated into two channels before entering the first quadrupole. (The magnetic design of the doublet quadrupoles is almost identical, whichever crossing plane is used.) On the one hand, the need for early beam separation is a relative disadvantage to doublet optics, since the need to include inboard beam splitting dipoles pushes the first quadrupole further away from the IP. On the other hand, early separation is good for the long range beam-beam effects, since there are (effectively) no parasitic collisions beyond the beginning of the first beam splitting dipole. In other words  $L_{sep} \approx L^* = 30$  m with flat optics, in the language of Equation 30. Flat beams therefore reduce both horizontal and vertical long range beam-beam tune shifts, with respect to the round beam alternative.

### 3.1.3 Intra beam scattering and diffusion

Intra beam scattering (IBS) is an important effect in the high field ring, as illustrated in Figure 19. The horizontal growth rate is by far the strongest, with growth times as small as about 7 hours after a couple of damping times, when the 6-dimensional phase space density is largest. This minimum growth time is controlled by heating the beams longitudinally, to maintain an rms momentum spread of  $\sigma_p/p \simeq 5 \times 10^{-5}$ , as demonstrated in Figure 14. It also helps that, in order to respect the beam-beam limit, the horizontal emittance is heated to maintain a minimum value of about  $\epsilon_x \approx 0.20 \mu\text{m}$ , much larger than the natural value of  $\epsilon_x = 0.04 \mu\text{m}$ .

According to our best current theoretical understanding, IBS is expected to be significant, but not dominant, in the high field ring of the VLHC [7]. The relative paucity of world data on IBS results in cautious predictions for the VLHC. Fortunately, the copious data expected in the next few years from RHIC operations should greatly improve our understanding of the topic. Any unwanted source of diffusion – whether IBS, power supply ripple, fundamental beam dynamics, or any unexpected source – could have a profound unwanted effect on the luminosity performance of the high field ring. A deep accelerator physics understanding of the spectrum of diffusion mechanisms is required for a confident high field design.

### 3.1.4 Luminosity versus energy

The High Field VLHC ring will be the first cryogenic collider to operate in the synchrotron radiation dominated regime, in which the radiation damping time is shorter than the storage time. In this regime there are practical and economic limits to the cryogenic system which can be installed. There is a maximum value  $P_{cryo}$  for the synchrotron radiation which can be absorbed in each ring. It is necessary to adjust the beam parameters to stay within the installed power limit, resulting in a maximum luminosity which depends on the beam energy  $E$  according to

$$L_{max} \propto \frac{P_{cryo}}{E} \quad (34)$$

The exact version of this “maximum power law” is derived as follows.

The total number of protons burnt off per beam, in a store time of length  $T_{store}$  in a collider with  $N_{IP}$  interaction points, is

$$N_{burn} = N_{IP} L_{ave} \sigma_{tot} T_{store} \quad (35)$$

where  $\sigma_{tot}$  is the total cross section and  $L_{ave}$  is the average luminosity. The number of protons in each beam at the beginning of the store must be at least this large, so

$$NM \geq N_{burn} \quad (36)$$

where  $N$  is the number of protons in each of the  $M$  bunches. The total synchrotron radiation power per ring is

$$P = \left( \frac{U_0}{T_{rev}} \right) NM \quad (37)$$

where  $U_0$  is the energy radiated per proton per turn, and  $T_{rev}$  is the revolution period. Table 13 records these and other related parameters. The synchrotron radiation damping time is closely related,

$$T_0 = \left( \frac{T_{rev}}{U_0} \right) E \quad (38)$$

so that, simply

$$P = \frac{NME}{T_0} \quad (39)$$

Putting all this together, and recognizing that the synchrotron power is limited

$$P < P_{cryo} \quad (40)$$

then the minimum synchrotron power is achieved when every single proton is burnt off, so that

$$L_{ave} < \frac{P_{cryo}}{E} \left( \frac{1}{N_{IP}\sigma_{tot}} \right) \left( \frac{T_0}{T_{store}} \right) \quad (41)$$

This is the exact form of the maximum power law.

Although there is a clear advantage in reducing the storage time,  $T_{store}$  must remain significantly larger than  $T_{damp}$  in order to take advantage of radiatively damped beam sizes. Other factors (such as the refill time) will also play a role in determining the optimum value of  $T_{store}$ , but is safe to estimate that

$$\frac{T_0}{T_{store}} \sim 0.2 \quad (42)$$

Except for some uncertainty in this factor, the maximum power law clearly states that the installed capacity to absorb synchrotron radiation at cryogenic temperatures directly limits the attainable product of average luminosity and energy.

Similarly, if the beam stored energy per ring  $U = NME$  must be kept below a maximum value – for example if the beam dump has a limited capacity – then

$$L_{ave} < \frac{U_{max}}{E} \left( \frac{1}{N_{IP}\sigma_{tot}} \right) \left( \frac{1}{T_{store}} \right) \quad (43)$$

Insofar as the stored energy is a practical limit to high field performance – to the product  $L_{ave}E$  – then there is pressure to reduce  $T_{store}$ , and hence to increase the dipole field, to reduce the circumference, and to reduce the refill time.

Energy loss per turn, $U_0$	15.3	MeV
Revolution period, $T_{rev}$	.778	ms
Damping time, $T_0$	2.48	h
Synch. rad. power, per beam $P$	1.05	MW
Dipole linear heat load	5.6	W/m
Stored energy, per beam $U$	4.7	GJ

Table 13: Synchrotron radiation related parameters.

### 3.2 Lattice optics (Tepikian)

The lattice for the high field (HF) ring is grouped into four units. The two hemispheres are made of arc cells. These two hemispheres are joined with two utility regions that contain dispersion suppressors, abort utility regions, interaction regions (IR), injection and extraction septa and kickers, et cetera. The lattice geometrically matches the low field (LF) ring lattice so that they both fit in the same tunnel. For convenience, a short list of some of the HF lattice parameters is shown in Table 14.

Horizontal tune	218.19	
Vertical tune	212.18	
Transition gamma	194.13	
Slip factor	$2.653 \times 10^{-5}$	
Maximum arc beta	459	m
Maximum arc dispersion	1.42	m
Rigidity at injection	$3.336 \times 10^4$	Tm
Rigidity at store	$2.919 \times 10^5$	Tm
Vertical $\beta^*$ (store)	0.37	m
Horizontal $\beta^*$ (store)	3.7	m
Maximum $\beta$ , injection	.614	km
Maximum $\beta_{max}$ , store	10.6	km

Table 14: Short list of some high field lattice parameters.

The first major module to describe is the arc cell. The half cell length is 135.4865 m. Both rings define optical modules with lengths in multiples of the half cell length. This is done to keep the geometries the same. Further requirements of the cell design are that the dipole magnetic length must be less than 17 m, and that spool pieces are required for correctors and sextupoles. The arc quadrupole gradient is restricted to 400 T/m and the maximum field of the dipole is 10 T. Furthermore, dual plane Beam Position Monitors (BPM) are placed between the quadrupole and spool piece. Table 15 shows the parameters for the arc cell and for for the dispersion suppressor cell.

The other major arc module is the dispersion suppressor. There are two types, one bringing the dispersion to zero and the other matching the zero dispersion regions to arc cell Twiss function values. The dispersion suppressor follows the “3/4, 2/3” rule, in which the cell length is 3/4 of the standard arc cell, and the bend angle is 2/3 of the standard arc cell. This is used to achieve maximum packing fraction. These two dispersion modules only differ in their quadrupole strengths.

The layout and parameters for arc and dispersion suppressor cells are shown in Figures 20 and 21, and their Twiss functions in Figures 22 and 23.

There are two utility regions. The one on the Fermilab site contains the abort insertion, Interaction Regions, et cetera. The off-site utility region is simply filled with FODO cells, with and without dipoles, and dispersion suppressors. Figure 24 displays the Twiss functions for the off-site utility region.

The IR gives 30 m free space from the interaction point to the first magnetic element. The first magnet encountered is a high field small bore magnet of 16 T field. This can handle the beams until they total separation becomes 8 mm. Then the beams enter a lower field, 12 T, magnet with a larger bore. These beam separation dipoles bend the beam vertically. This crossing region requires that the beam separation at the first quadrupole be 30 mm. With these dimensions the first quadrupole is limited to 400 T/m gradient. As the beams separate, a higher quadrupole field can be attained with a limit of 600 T/m. A schematic of this design is shown in Fig. 25.

With this design of the crossing region, an IR is designed to fit at two location in the on-site utility region. The  $\beta^*$  was varied from 0.37 m to 7.12 m (vertically,  $\beta^*$  horizontally is 10 times larger). The maximum beta  $\hat{\beta}$  is 10.6 km with the collision optics and only about 760 m at injection. Figure 26 shows the  $\beta^*$  squeeze every 0.25 m. Figure 27 shows the injection and collision optics of the interaction region. Note that, due to the vertical crossing dipoles there is vertical dispersion throughout the ring. This will be dealt with as the design of the insertion progresses. Furthermore, the phase advance across the insertion has not been fixed. There are additional quads that can be varied to fix the phase advance. The abort region has yet to be designed.

DIPOLE		
Field at injection	1.116	T
Field at store	9.765	T
Bend radius	29.887	km
Coil full width	40	mm
Liner full width	20	mm
Vertical bore separation	.29	m
Stored energy (2 bores)	828	kJ/m
CORRECTORS		
Corrector magnetic length	1.0	m
Dipole corrector max strength	4.0	Tm
Skew quad max strength	141	T
Sextupole max strength	6000	T/m
ARC CELLS		
Half cell harmonic	24	
Half cell length	135.486	m
Half cell bend angle	3.875	mrاد
Half cell count	1568	
Dipoles per half cell	7	
Dipole count, total	10976	
Dipole magnetic length	16.546	m
Dipole fill factor	85.5	%
Quad magnetic length	8.066	m
Quad field gradient	385.4	T/m
DISPERSION SUPPRESSOR CELLS		
Half cell harmonic	18	
Half cell length	101.614	m
Half cell bend angle	2.583	mrاد
Half cell count	80	
Dipoles per half cell	5	
Dipole count, total	400	
Dipole magnetic length	15.443	m
Dipole fill factor	76.0	%
Quad magnetic length	10.775	m
Quad field gradient (QD1)	288.7	T/m
Quad field gradient (QF2)	376.2	T/m
Quad field gradient (QD3)	281.9	T/m
Quad field gradient (QF4)	390.2	T/m

Table 15: Arc and dispersion suppressor magnet and cell parameters.

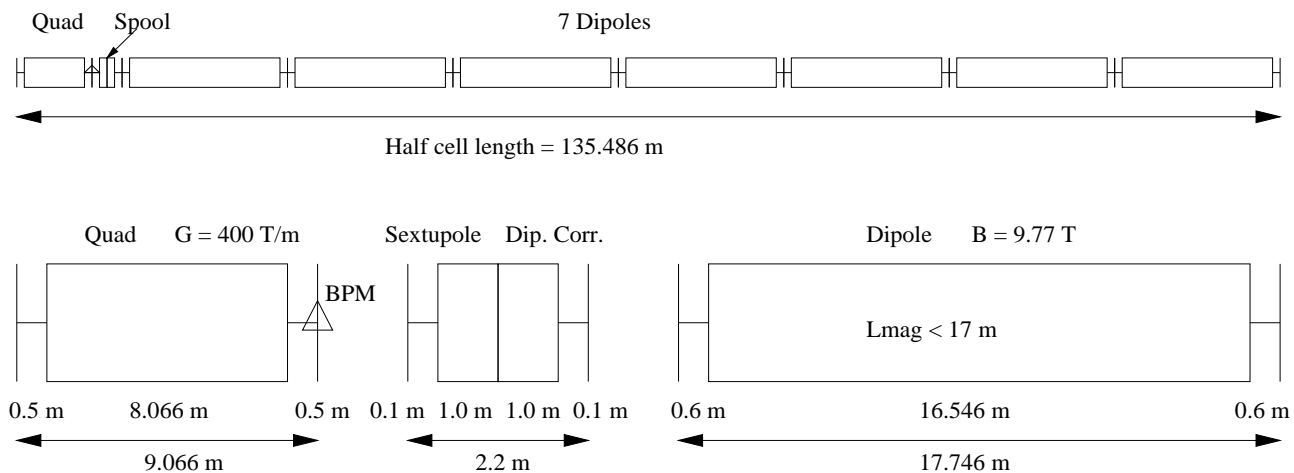


Figure 20: Layout and parameters of a high field arc half cell.

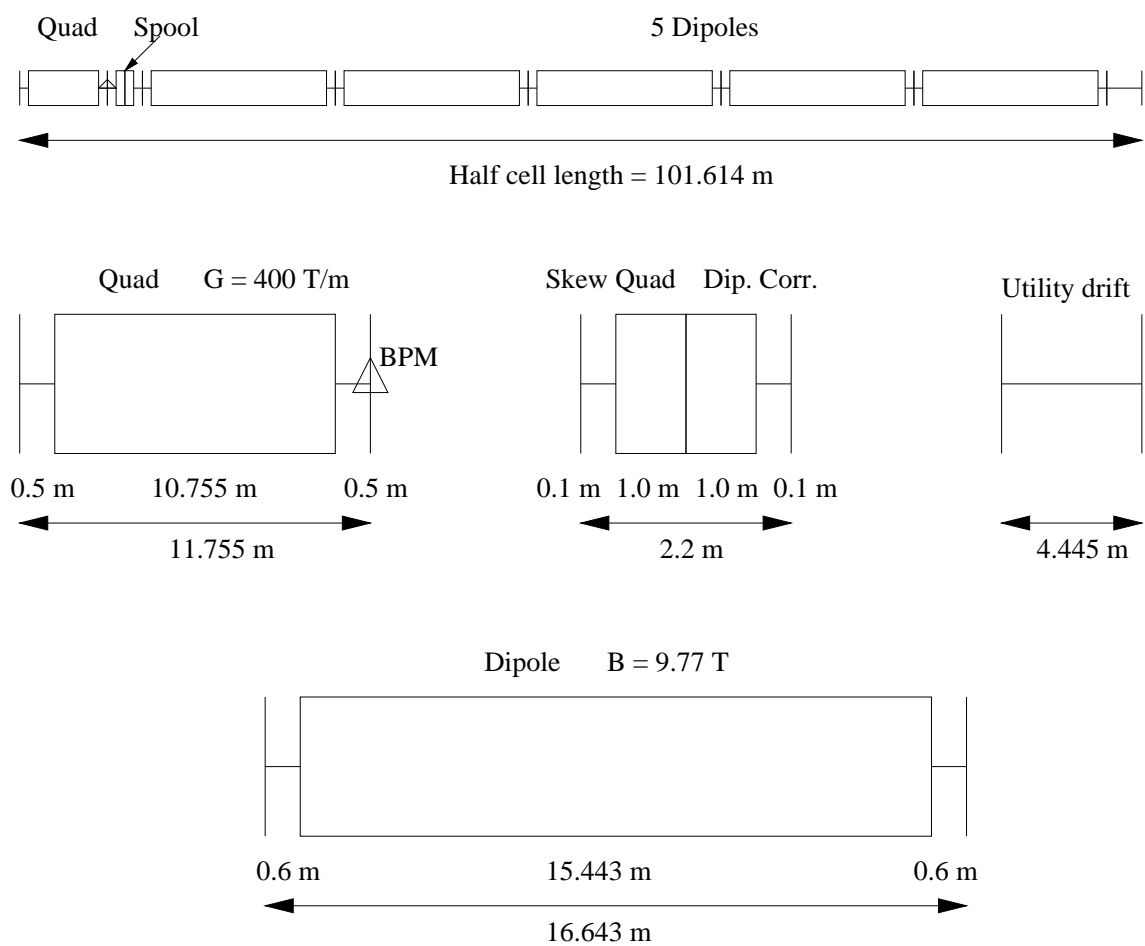


Figure 21: Layout and parameters of a high field dispersion suppressor half cell.

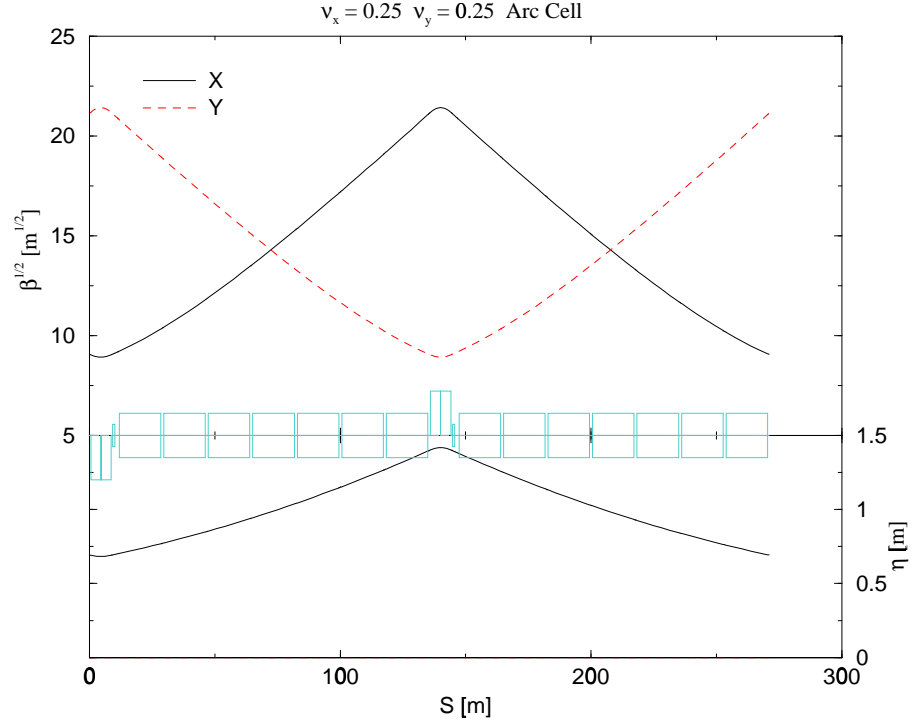


Figure 22: The arc cell Twiss functions. The beam line is shown with the dipoles, spool pieces and the quadrupoles.

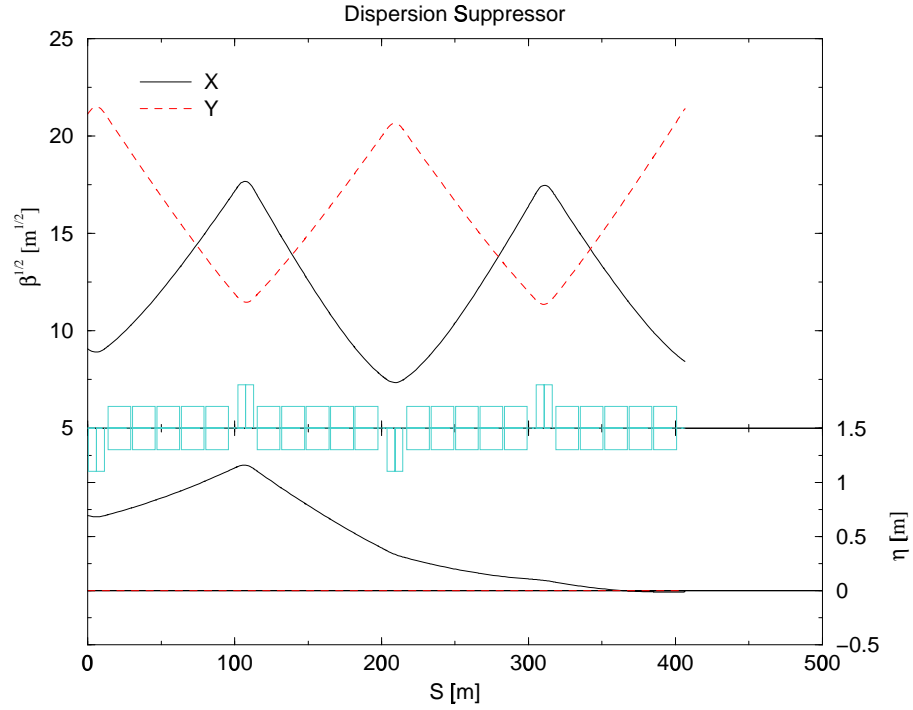


Figure 23: The dispersion suppressor Twiss functions. Each half cell is  $3/4$  the length of the arc half cell, so the total length is 3 arc half cells long.

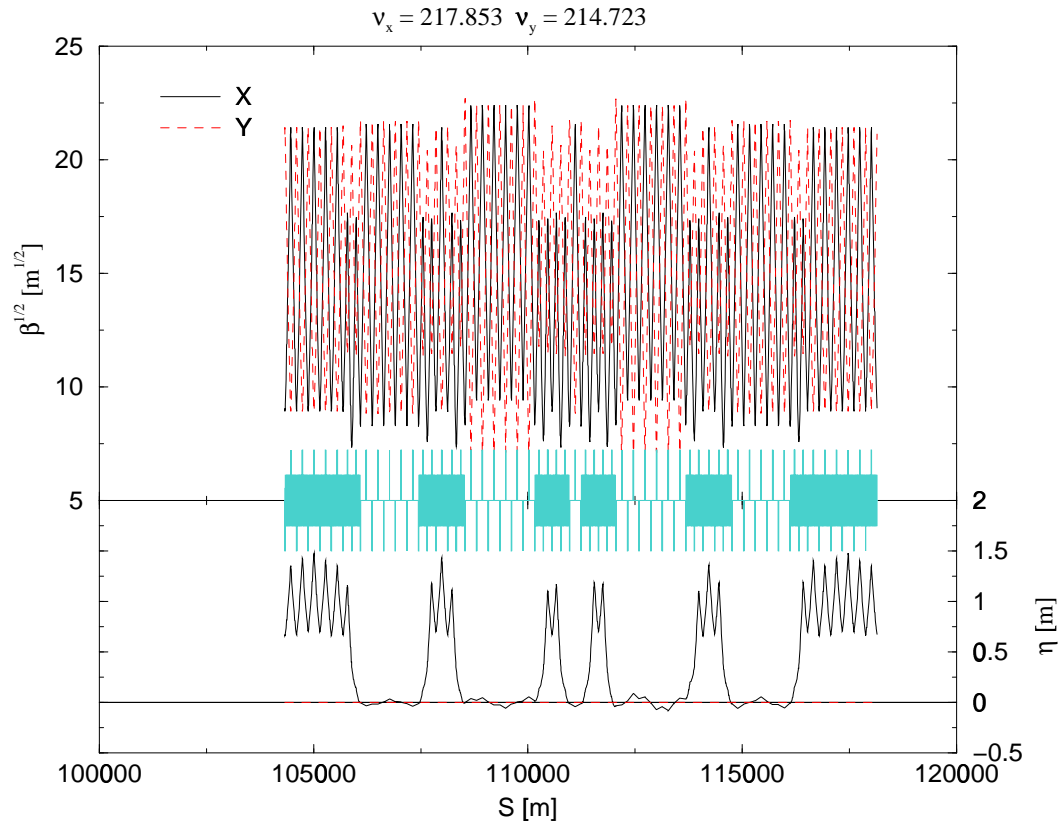


Figure 24: Twiss function in the off-site utility region on the far side of the ring from the Fermilab site.

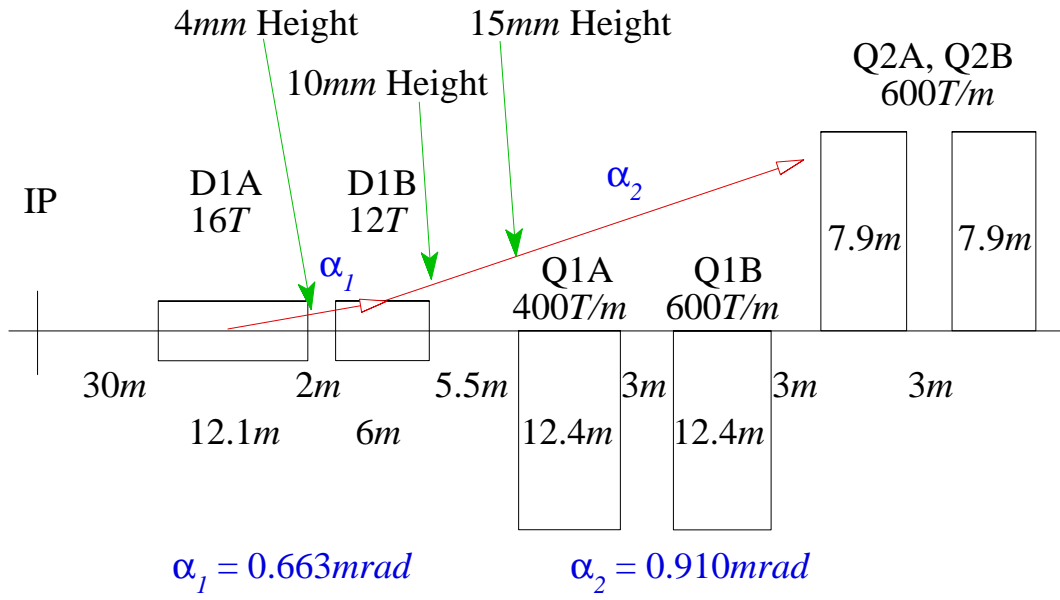


Figure 25: The IR layout. Shown here is the first crossing point dipoles and the doublet quadrupoles Q1 and Q2. Note, the quadrupoles are split into two pieces to provide space for correctors. The beam angles and height relative to the central line are shown. Note, the beam separation is twice the height.

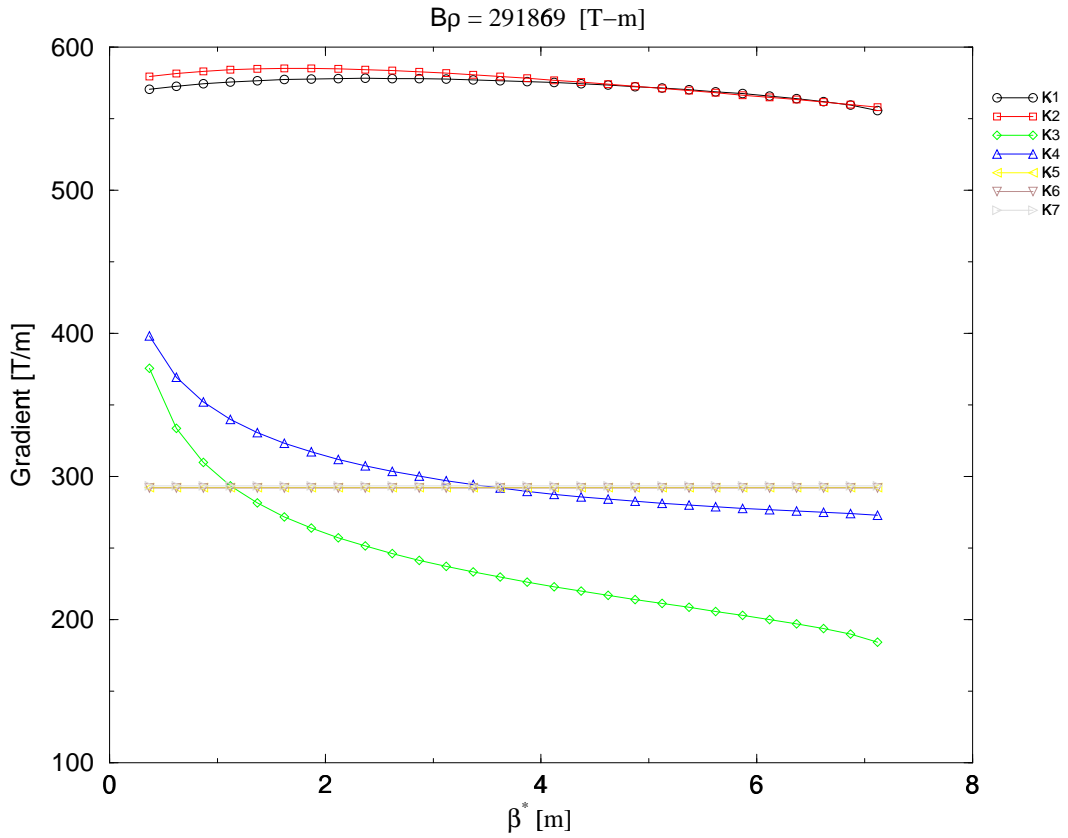


Figure 26: Words west

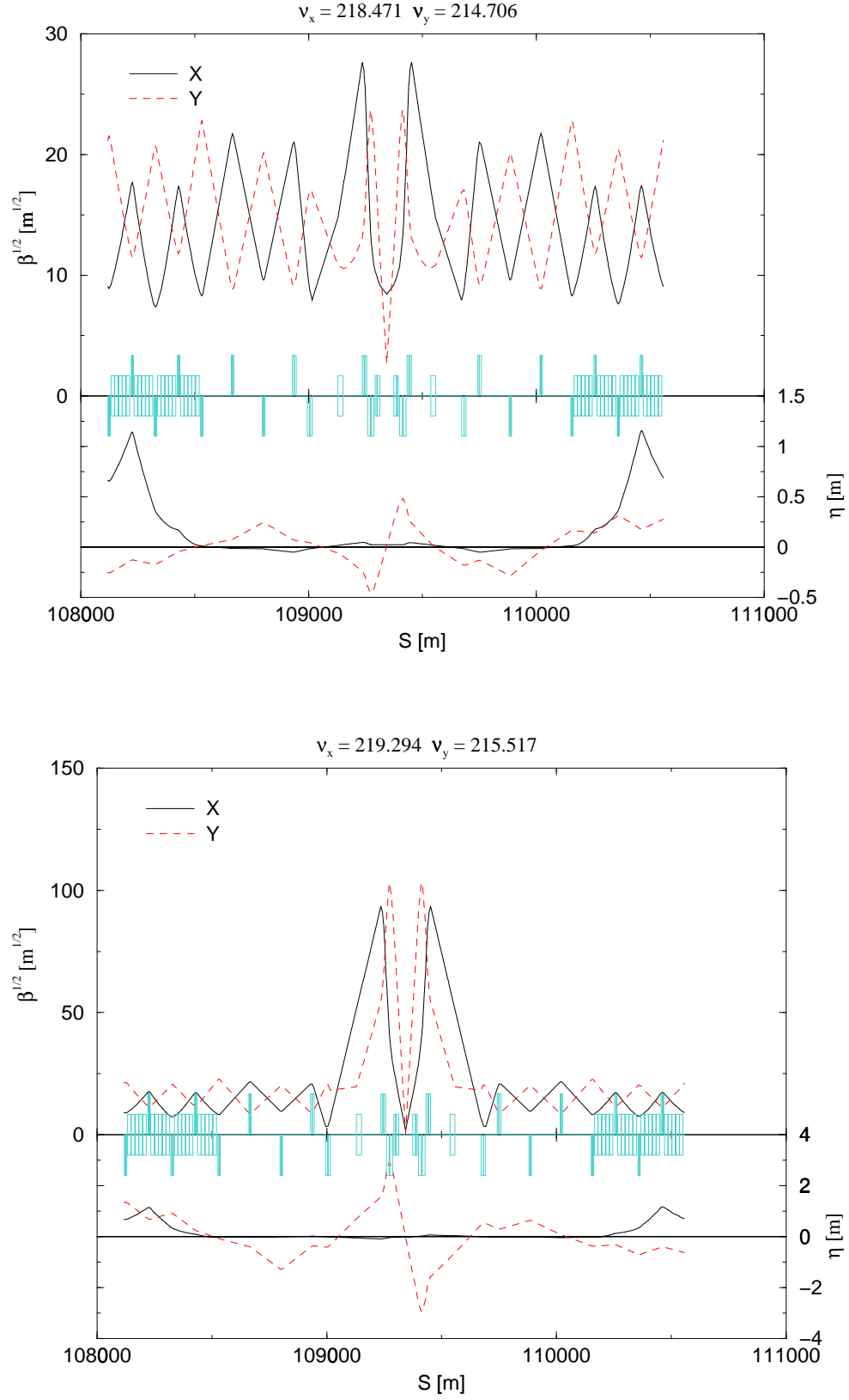


Figure 27: Twiss functions at one of the IPs in the injection optics (top) and in the collision optics (bottom).

### 3.3 Magnet aperture and field quality (Fischer)

The effect of the magnetic field quality on the dynamic aperture was investigated at the injection energy of 10 TeV. At injection the beam size has its maximum and errors in the arc magnets dominate the dynamic aperture. With the current one-turn injection scenario, a storage time in the order of seconds is sufficient.

To estimate the effect of the magnetic field errors on the single particle dynamic, the nonlinear chromaticity, the tune spread from nonlinear fields and the 1000-turn dynamic aperture were computed. 1000 turns is equivalent to 0.7 seconds real time in the VLHC.

Experiments have shown that the dynamic aperture can be computed for storage rings with nonlinear field errors within a 30% error when the field errors are well known [13, 14]. For a future machine, however, a larger safety margin is required.

In the lattice that is used for the evaluation, no interaction regions were inserted since the dynamic aperture is dominated by the arcs. Arc magnet error tables version 1.0 were used (see Tabs. 30 and 31). In these tables, field errors at injection were estimated for a 2.0 T field in the dipoles. However, an injection of a 10 TeV beam would correspond to a 1.4 T field in the dipoles. The difference in the main field should not affect field errors caused by geometry. Only the sextupole component in the dipoles, caused by coil magnetization, is expected to be materially different. The systematic errors were computed as the maximum possible absolute value with given mean and uncertainties. Random errors were created from a Gaussian distribution, cut at two sigma.

Quadrupoles were horizontally and vertically displaced randomly with a Gaussian distribution with a 0.3 mm rms value, cut at three sigma. In addition, beam position monitors were displaced with a 0.2 mm rms value. The resulting non-zero closed orbit was corrected to zero in the beam position monitors with horizontal orbit correctors at focusing quadrupoles and vertical orbit correctors at defocusing quadrupoles. Skew quadrupole errors in the arcs were disregarded and no coupling correction was necessary. The transverse tunes were set to (218.190, 212.180). Both horizontal and vertical chromaticity were set to 2.

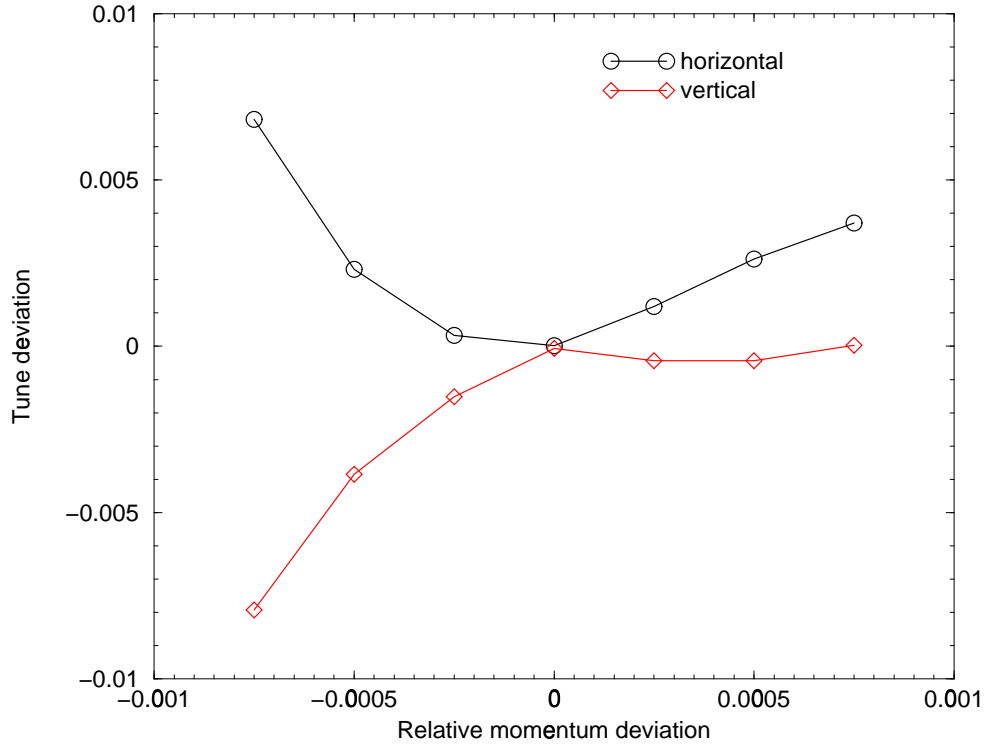


Figure 28: Horizontal and vertical tune as a function of the relative momentum deviation at 10 TeV.

In Fig. 28 the horizontal and vertical tunes are shown as a function of the relative momentum deviation. With relative momentum deviations of up to 0.00072, the tunes shift by up to 0.008.

Fig. 29 shows the tune space needed for on-momentum particles with betatron amplitudes of up to 6 sigma of

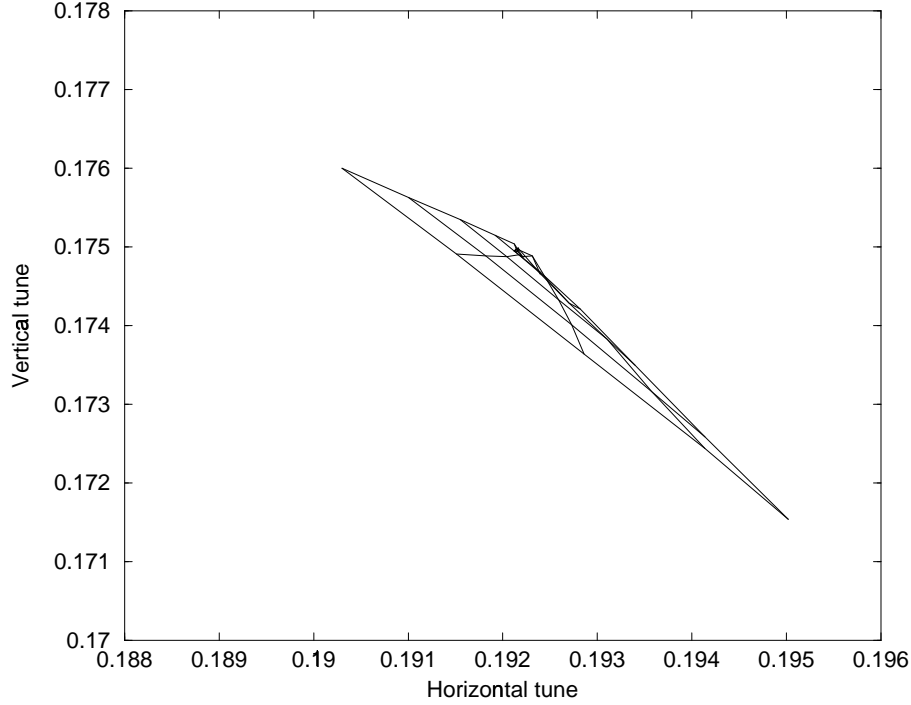


Figure 29: Tune space needed for on-momentum particles with betatron amplitudes of up to 6 sigma of the transverse rms beam size.

the transverse rms beam size. Five different ratios of horizontal to vertical emittance were chosen for this plot. The size of the needed tune space is dominated by the systematic octupole error in the dipole. This is shown in Fig. 30 where the systematic octupole errors were set to zero.

To determine the dynamic aperture, particles were tracked over 1000 turns (0.7 seconds real time). 10 different random distributions (“seeds”) of magnetic field errors were investigated. The total transverse emittance was distributed onto the horizontal and vertical emittance in 5 ratios:

$$\epsilon_x = 0.96 \cdot \epsilon_{total} \quad \epsilon_y = 0.04 \cdot \epsilon_{total} \quad (44)$$

$$\epsilon_x = 0.75 \cdot \epsilon_{total} \quad \epsilon_y = 0.25 \cdot \epsilon_{total} \quad (45)$$

$$\epsilon_x = 0.50 \cdot \epsilon_{total} \quad \epsilon_y = 0.50 \cdot \epsilon_{total} \quad (46)$$

$$\epsilon_x = 0.25 \cdot \epsilon_{total} \quad \epsilon_y = 0.75 \cdot \epsilon_{total} \quad (47)$$

$$\epsilon_x = 0.04 \cdot \epsilon_{total} \quad \epsilon_y = 0.96 \cdot \epsilon_{total} \quad (48)$$

No synchrotron motion was included but particles had a relative momentum deviation of  $\Delta p/p = 7.2 \cdot 10^{-4}$ , corresponding to three times the rms of the momentum distribution. The physical aperture of 1 cm in the arcs corresponds to 35  $\sigma$  of the transverse beam size in the quadrupoles.

Fig. 31 shows dynamic aperture averaged over the 10 seeds along with the minimum of the 10 seeds. The error bars of the average dynamic aperture are the rms value of 10 seeds.

Although linear coupling and synchrotron motion were disregarded in the determination of the dynamic aperture, the field quality with the magnet field error table V1.0 is sufficient for injection. In addition, A reduction in the systematic octupole error in the dipole is likely to yield a further gain in dynamic aperture since this field error dominates the tune spread from nonlinear magnetic field errors.

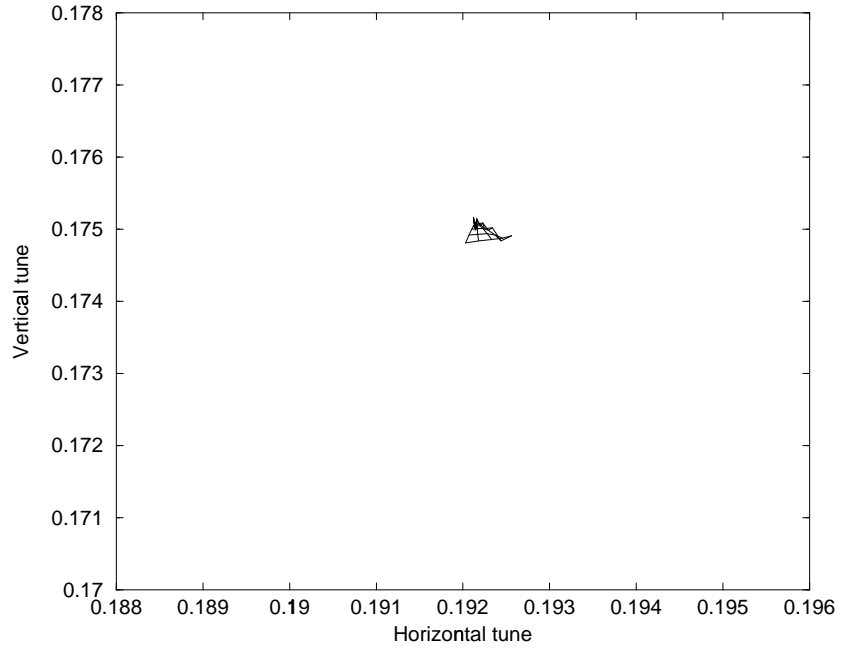


Figure 30: Tune space needed for on-momentum particles with betatron amplitudes of up to 6 sigma of the transverse rms beam size, without systematic octupole errors in dipoles.

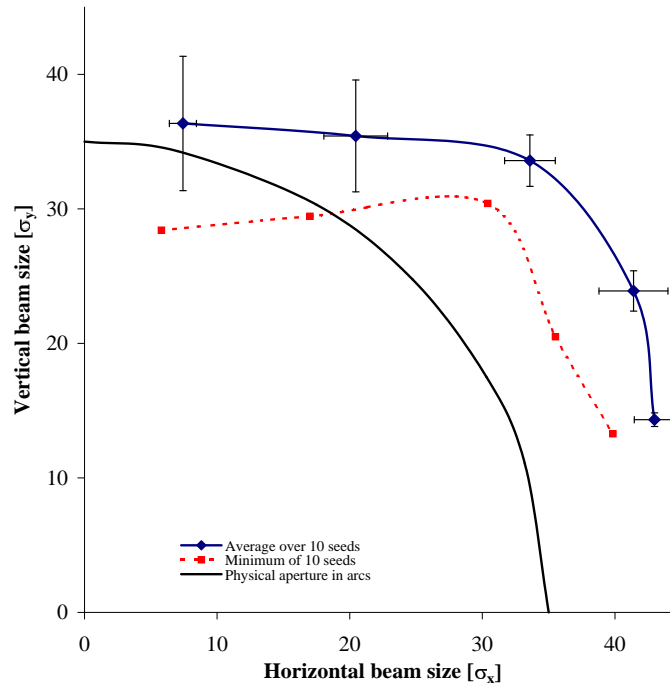


Figure 31: 1000-turn dynamic aperture. Shown are the average over 10 seed, the minimum of 10 seeds and the physical aperture, in in units of the transverse rms beam size. The error bars of the average dynamic aperture are the rms value of 10 seeds.

### 3.4 Tolerances (Ptitsyn)

In this section we consider the effect of magnet misalignment as well as the effect of main dipole and quadrupole field errors on the beam orbit and betatron tunes. On the basis of these considerations we then derive the tolerances for misalignment and field errors. To this purpose we use the VLHC high-field optics with  $\beta_x^* = 3.7\text{m}$  and  $\beta_y^* = 0.37\text{m}$ .

#### 3.4.1 Orbit errors

Possible sources of orbit error include transverse quadrupole misalignments (in both the horizontal and vertical directions), main dipole field integral errors (for the horizontal orbit), and roll of the main dipole magnets (for the vertical orbit). In order to estimate and compare the value of the orbit distortion coming from these different types of error sources, the rms closed orbit has been calculated. The calculations assumed a rms magnet misalignment of  $200\text{ }\mu\text{m}$ , an rms magnet roll of  $1\text{ mrad}$ , and an rms field integral error of  $10^{-4}$ . Two cases were considered. In the first the errors are introduced in all magnets in the accelerator arcs, while in the second the errors are applied to the quadrupoles of one of the interaction region doublets. The calculated results are summarized in Table 16. Horizontal (X) and vertical (Y) rms orbit values characterize the contribution coming from different perturbation sources. The corrector strengths required to compensate for the perturbations from different sources are also listed. The strength was calculated assuming that in the arc regions horizontal correctors are placed next to each focusing quad and vertical are next to defocusing quads. In the interaction regions there is one corrector per plane in the doublets.

Error type	X orbit rms [mm]	Required X strength, 2.5 rms, [Tm]	Y orbit rms [mm]	Required Y strength, 2.5 rms, [Tm]
IR Quad offset $200\text{ }\mu\text{m}$	9	3.4	12	3.4
Arc Quad offset $200\text{ }\mu\text{m}$	27	1.4	27	1.4
Arc dipole roll $1\text{ mrad}$			10	0.5
Arc dipole field error $10^{-4}$	1.13	0.06		
IR dipole field error $10^{-4}$	0.13			

Table 16: RMS horizontal and vertical dipole correctors strengths required to correct the closed orbit under the influence of different error sources.

The relative dipole integral field error of  $10^{-4}$  provides a much smaller contribution to the horizontal orbit perturbation than the quadrupole misalignment. The effect of the dipole roll is more pronounced, and so reducing the dipole roll tolerance to  $0.5\text{ mrad}$  seems advisable.

Adding the rms corrector strengths required to combat all error sources in quadrature, and multiplying by 2.5, a value of  $3.7\text{ Tm}$  integrated strength is attained for the arc dipole correctors, and  $8.5\text{ Tm}$  for the IR dipole correctors. This maximum strength for the IR correctors is nominally too large, and so reducing the tolerance for the IR quadrupole misalignment to  $100\text{ }\mu\text{m}$  seems advisable.

#### 3.4.2 Tune error, coupling and IR chromatic effects

The betatron tune shift caused by an rms quadrupole field error of  $10^{-4}$  and the betatron coupling effect produced by rms quadrupole rolls of  $1\text{ mrad}$  have been calculated. Table 17 shows the effect produced by quadrupole gradient errors. The errors coming from arc quadrupoles are small enough that a  $10^{-4}$  tolerance for the arc quadrupoles is clearly too tight. The error in interaction region quadrupoles can be corrected by adjusting the currents of power supply for these quads.

The coupling effect produced by quadrupole roll is shown in Table 18. Both a global coupling correction system in the arcs and a local skew-quadrupole correctors in the interaction regions are required for the compensation of the coupling effect. A challenging tolerance for the IR quadrupole roll would be  $0.1\text{ mrad}$ . The tolerances for the arc quadrupole rolls should be calculated with the knowledge of the coupling correction system realized in the ring. The scaling done from the RHIC coupling correction system provides  $0.2\text{ mrad}$  the roll tolerance value.

$\Delta K/K = 10^{-4}$	$\Delta Q [10^{-3}]$	$\Delta\beta/\beta [\%]$
All arc quads	1.15	0.75
IR doublet quads	3.	3.26

Table 17: Quadrupole gradient errors

Quad roll= 1mrad	$\Delta Q_{min} [10^{-3}]$
All arc quads	11.5
IR doublet quads	30.

Table 18: Betatron coupling effect

Because of the very large maximum  $\beta$  values in the interaction region quadrupoles, especially the vertical  $\beta_y^{max} = 10.6$  km, the chromatic effects produced by these quadrupoles have been evaluated. For the design value of rms momentum spread of  $5 \times 10^{-5}$  the amplitude of chromatic vertical beta-wave was found to be just a few percent. Thus the effect is not large, mainly due to the small value of rms momentum spread. The vertical chromaticity produced by the quadrupoles from one interaction region has been found to be about -42. The horizontal chromatic effects are smaller than in the vertical.

### 3.4.3 Tolerance summary

Table 19 summarizes the offset and roll tolerances for VLHC magnets recommended in this section. All the numbers listed in the table apply to quadrupole misalignments. Tolerances for dipole magnets are not so critical and can be relaxed by a factor 2 or even more.

The tolerances for the magnet offset are quite small. They are directly related to the available strength of the corrector system. The arc dipole correctors are required to have 4 Tm maximum strength while the correctors in the interaction regions should be up to 5 Tm. Even this dipole corrector strength can not make up for the magnet offset diffusion caused by the ground motion that is described elsewhere in this report. Ground motion might put magnet offsets well beyond the defined tolerances after few years of movement. Thus, periodic magnet realignment will be necessary.

ERROR	ARCS	IRs
Offset, mm	0.2	0.1
Roll, mrad	0.2	0.1

Table 19: Tolerance summary for magnet alignment

## 3.5 Corrections (Pilat)

The high field VLHC collider is a machine that relies on powerful diagnostics and correction systems to reach its ultimate performance, similarly to existing and planned hadron colliders like RHIC and the LHC. Static corrections of trajectory, orbit, optical errors and distortions are required as well as dynamic corrections of machine characteristic during ramping and beta squeeze. The effectiveness of feedback systems has to be evaluated with respect of the tightening of tolerances. In the present chapter we will specify a correction system for VLHC on the basis of the

error tolerances worked out for the VLHC itself and experience from recently built or designed hadron colliders. The following two sections describe the arc correction system, and the special correction requirements of the interaction regions.

### 3.5.1 Arc correction system

The arc correction system consists of an orbit correction system, a coupling correction system and a chromaticity correction system. The correction plan is to use the arc systems to correct the injection configuration, with enough strength to propagate the corrections to top energy. Additional errors and effect arising from the collision optics and configuration are addressed by the Interaction region (IR) system. This strategy has been successfully used in RHIC. Preliminary simulation results with the VLHC injection optics and predicted field imperfections lead to the conclusion that there is no need for nonlinear correctors in the arc cells other than the chromaticity sextupoles. The orbit correction system consists of dipole correctors placed next to each arc quadrupole. The configuration of the arc corrector packages (dipole, sextupole), the specifications for the corrector dipoles and the tolerances were already discussed in the previous chapters. Automatic orbit correction, based on a menu of algorithms, will be provided, based on fast orbit acquisition from the beam position monitor system, including turn-by-turn acquisition. Sextupole correctors are also part of the arc corrector package, to statically compensate the chromatic effect and dynamically compensate for time dependent effect in the magnets.

For the correction of coupling the proposed solution has the skew quadrupoles located at QF and QD positions in the dispersion suppressor cells, in the 2 utility regions in the interaction region areas. The skew quadrupole replace the sextupole corrector in the arc correction package configuration, for a total of 80 skew quadrupole correctors per ring. The skew quadrupoles can be connected in up to 4 families, which allows flexibility in choosing the method for coupling compensation. The system specifications have been determined by evaluating the leading source of coupling in the arcs, the roll misalignment error in the arc quadrupoles, and allowing some margin for the compensation of skew quadrupole error fields in the dipoles.

The specification for the skew quadrupole integrated strength in the corrector package, 141 T, has been used to compare the performance of the VLHC skew quadrupole correction system to the similar RHIC system. As a figure of merit, we take  $R = (\text{total skew corrector strength}) / [\sqrt{N} * (\text{arc quad strength})]$  with the numerator being the total skew corrector strength available in the machine and the denominator proportional to the minimum tune separation generated by a distribution of random roll errors in the arc quadrupoles.

The ratio for RHIC (with 1.5 T integrated strength in the skew quadrupoles, 48 skew quadrupoles per ring, and 276 arc quadrupoles at 7.81 T each) is 0.56. For the VLHC (80 skew quadrupoles at 141 T and 784 arc quadrupoles, 8 m long and a gradient of 400 T/m) the ratio is 0.13, about a factor 4 from RHIC. Given that the roll misalignment specification for RHIC is 1 mrad in the arc quadrupoles, the proposed skew correction system of the VLHC can adequately compensate a random alignment error in the arcs quadrupoles of 200  $\mu\text{rad}$ , with some margin for other sources of arc coupling. Coupling effects arising from the interaction regions are corrected with the IR decoupling system and will be discussed in the next section.

### 3.5.2 Interaction region correction system

The goal of the IR system is to locally correct for effects and errors arising from the interaction regions. The fact that the effect of the IRs is most relevant in collision optics, when the focusing at the interaction point (IP) and the beat functions in the IR final focus quadrupoles are maximized, is what makes this correction modularity possible. The independent and local correction of IR effects has been a guiding principle in the design of RHIC and the LHC.

The IR correction systems can be functionally divided in linear and nonlinear, but the implementation often favors integrated solutions, like multi-layer correction packages, given the tight constraints on space near the IP. The schematics for the proposed IR correction system is displayed in Figure 32.

Figure 32: Not yet functional.

Two correction packages are placed in the 3 m drifts between the two doublet quadrupoles, a skew package between Q1A and Q1B, and a normal package between Q2A and Q2B to take advantage of the beta functions. A detailed magnetic design of the IR region correction system is in progress, so the specifications are driven from the requirements and extrapolation from the correction package designed for the arcs. The linear correction system

consists of 2 dipole correctors and 1 skew quadrupole layer. The dipole correctors provide orbit control, IP and crossing angle control. An integrated strength of 5 Tm will correct for an rms displacement in the doublet of 100  $\mu\text{m}$ . Feedback on beam position at the IP and on the crossing angle may be required and will be addressed in the future.

The skew quadrupole corrector is used to compensate locally the residual coupling from the final focus doublet quadrupoles. An integrated strength of 141 T will be able to compensate for a residual misalignment of 0.1 mrad. This tolerance is set on the basis of extrapolation from LHC and SSC, and calculated contribution to the minimum tune separation.

The nonlinear correction system is modeled after the design of the RHIC and LHC systems, adapted to the doublet optics configuration, and with consideration to the design of the VLHC doublet quadrupoles. A local sextupole, octupole and a dodecapole corrector are part of the normal corrector package, and a skew sextupole and octupole are in the skew package. The choice of layers is dictated by previous experience with RHIC and LHC and from preliminary values of the doublet harmonics. A more detailed study will be necessary to validate these choices and to determine the strengths of the nonlinear correction layers. With the present technology a 4-layer corrector is at the limit of feasibility. Should additional or stronger correctors be necessary, they can be installed in the drift between Q1B and Q2A or between Q2B and D2.

The VLHC IRs with the nominal optics contribute -42 units of vertical chromaticity to a machine that has a natural chromaticity in excess of -200 units. The need for a local chromaticity compensation system to correct for the second order chromaticity from the IRs will have to be addressed. To this end the sextupole corrector at the doublet is useless since it is in a zero dispersion location. Should IR second order chromaticity compensation be necessary that can be achieved with 2 families of sextupoles placed in the arc region adjacent to the IRs. The first family SX1 compensates the second order IR chromaticity, the second family SX2 is necessary to suppress the first order chromaticity contributed by SX1.

Double plane beam position monitors (BPMs) are essential in the interaction region and they have to be included in the planning from the start. The BPM in front of D1A is the main tool to monitor the IP and must have capability of observing both beams. The other BPMs are used for orbit and crossing angle monitoring.

### 3.6 Beam stability (Blaskiewicz)

Table 20 lists fairly well known parameters relevant to beam stability. Unknown parameters include the broad band impedance as well as narrow band parasitic impedances. For the latter quantities the stability calculations will be used to obtain safe limits.

PARAMETER	INJECTION	INITIAL STORE
circumference	$2\pi R = 233\text{km}$	
kinetic energy	10TeV	87.5TeV
RF Voltage	50MV/turn	200MV/turn
RF frequency	488MHz	
synchrotron frequency	$f_s = 3.48\text{Hz}$	$f_s = 2.35\text{Hz}$
rms bunch length	$\sigma_t = 0.273\text{ns}$	$\sigma_t = 0.112\text{ns}$
nominal betatron tunes	$Q_x = 218.19, Q_y = 212.18$	
beam pipe radius	$b = 1\text{cm}$	
rms normalized transverse emittance	$1.5\mu\text{m}$	$1.5\mu\text{m}$
nominal chromaticity	$Q'_x = \pm 2, Q'_y = \pm 2$	$Q'_x = \pm 2, Q'_y = \pm 2$
revolution frequency	$f_0 = 1.286\text{kHz}$	
$\gamma_t$	194.13	194.13
rms longitudinal emittance	$\pi\sigma(E)\sigma(t) = 2.0\text{eV}\cdot\text{s}$	
bunches for symmetric fill	$M = 41280$	
protons/bunch	$9.0 \times 10^9$	

Table 20: Parameters relevant to beam stability.

Start by considering the situation at injection energy. Transverse coupled bunch stability is largely determined by the resistive wall impedance. With its large circumference the relevant frequency range for VLHC starts at  $\sim 1\text{kHz}$ . The skin depth is given by

$$\delta = \sqrt{\frac{2\rho_e}{\mu|\omega|}} \quad (49)$$

where  $\rho_e$  is the electrical conductivity,  $\mu$  is the magnetic permeability, and  $\omega = 2\pi f$  is the angular frequency, with all quantities in MKS. For pure copper at 80K the electrical resistivity due to phonon scattering is  $\rho_e = 1/\sigma_c = 1.6 \times 10^{-9}\Omega\text{m}$  [17]. There is an additional component to the resistivity due to impurity scattering which remains to be determined. For cold stainless steel (SS) the conductivity is  $\rho_s = 1/\sigma_s = 7.3 \times 10^{-7}\Omega\text{m}$  [18]. For a frequency of  $f = 1\text{kHz}$  the skin depth in cold copper is  $\geq 0.64\text{mm}$ , while for cold SS it is  $1.4\text{cm}$ . The  $\geq$  for the copper is due to neglecting impurity scattering. To reduce uncertainties the copper lining will be neglected and the resistive wall transverse impedance it taken to be

$$Z_{\perp, rw} = \frac{Rc(1 - i\text{sgn}(\omega))}{2\omega b^3 \sigma_s \delta_s}, \quad (50)$$

where we have assumed a time dependence  $\propto \exp(-i\omega t)$ . Note that the resistive wall impedance will probably dominate the transverse impedance so calculating the effect of the copper liner should take precedence over estimating the impact of the myriad small additions to the transverse impedance.

The coherent betatron frequency in the weak coupling limit of the Wang formalism [19] is

$$\Delta Q_m = m\omega_s - i \frac{\bar{I}c}{4\pi 2^{|m|} |m|! (E_T/q) Q_\beta} \sum_{n=-\infty}^{\infty} Z_{\perp} [(nM + s)\omega_0 + \omega_\beta] e^{-\tilde{n}^2 \sigma^2} (\tilde{n}\sigma)^{2|m|}, \quad (51)$$

where  $m = \dots, -1, 0, 1, \dots$  is the synchrotron mode number,  $\omega_s$  is the angular synchrotron frequency,  $\bar{I}$  is the average current,  $M$  is the number of bunches,  $s$  is the coupled bunch mode number,  $E_T/q$  is the total proton energy divided by its charge,  $\sigma$  is the rms bunch length in units of machine azimuth,  $\tilde{n} = nM + s + Q_\beta - Q'_\beta/\eta$ , and  $\eta = 1/\gamma_T^2 - 1/\gamma^2$  is the slip factor.

Equation (51) assumes  $M$  identical, equally spaced bunches so it neglects the effect of the abort gap. This is a standard formula that can be found in ZAP, Chao's book, or any number of papers. Figure 33 shows the real (dQr) and imaginary (dQi) parts of the tune shift for  $m = Q'_\beta = 0$  at the injection energy.

The maximum growth rate with  $Im(\Delta Q_0) = 0.05$  occurs for the lowest negative sideband which would have an observed frequency of  $0.8f_0 = 1.03\text{kHz}$ . The growth rate of  $0.4/\text{ms}$  corresponds to an e-folding time of 3.2 turns. This mode and several other low frequency modes need to be damped. Following Marriner's suggestion [20] assume a transverse pickup which is low pass filtered, amplified, and applied to a kicker  $1/4$  of a betatron wavelength downstream. For low frequencies, beam position monitors differentiate the input signal, which is the product of the instantaneous current with the offset. A simple model produces the effective transverse impedance

$$Z_{\perp, d}(\omega) = -Z_c \frac{if}{f_0} \left( \frac{1}{1 - if/f_d} \right)^2. \quad (52)$$

Setting  $f_d = 5\text{kHz}$ , and choosing  $Z_c$  so that the fastest damped mode has  $dQi = -0.4$ , in the absence of the resistive wall impedance, yields the growth shown in Figure 34. With the damper, the growth rate of the most unstable mode is a factor of 20 smaller than with no damper. It is assumed that a bunch by bunch damper with one turn delay, or similar device, can take care of any residual, rigid mode, coupled bunch instability.

Next consider the fast head tail instability. This is done by choosing a tune  $Q_y = 212.5$  with  $M = 41281$  and  $s = 20428$ . These numbers satisfy  $s + Q_y - M = -(s + Q_y)$  which gives growth rates identically equal to zero for the weak coupling limit. In this case instability occurs when the impedance causes the coherent frequencies of adjacent synchrotron sidebands to collide. The formulas may be found in [21]. They appear to be identical to the MOSES code [22] but no direct check has been performed. Figure 35 shows the fast head-tail threshold at injection energy. The design current is safe by about a factor of 2 even with the assumption of no copper liner. With the copper liner the tune shifts should be substantially smaller so an rf voltage of  $50\text{ MV/turn}$  is probably fine.

The last transverse instability to consider is the normal head-tail instability. We limit our attention to modes that are damped by the low frequency damper, using  $s = -220$  as a test case. Using the weak coupling formulas there is

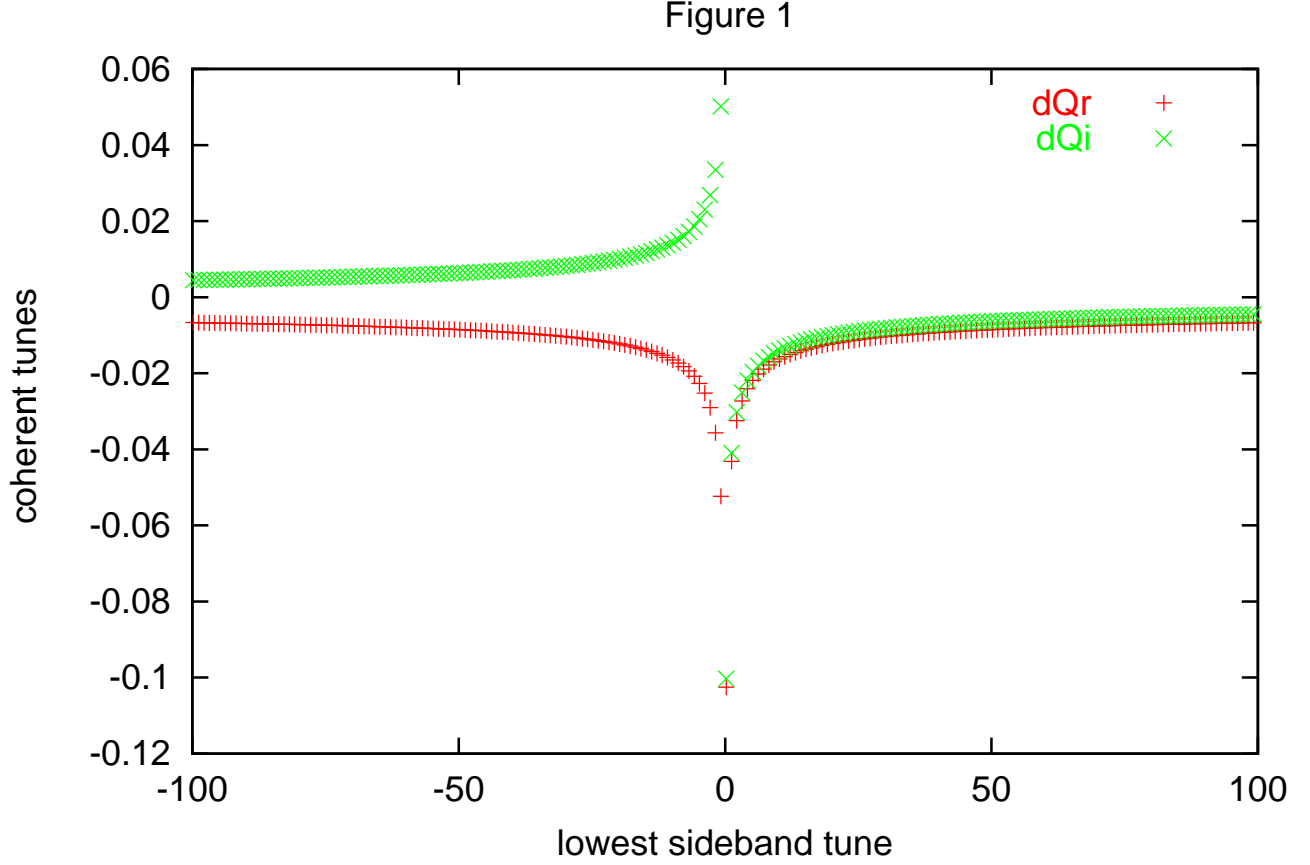


Figure 33: coherent tunes for  $m=0$  at 10 TeV versus observed frequency of lowest betatron sideband in units of the revolution frequency (1.29kHz). There is no damper.

no instability predicted for  $0 \leq Q'_y \leq 2$  at injection energy, which agrees well with experience. With mode coupling between the 3 lowest synchrotron modes, as per Figure 35, the same range of chromaticities are, again, stable. With coupling between the 6 modes with  $|m| \leq 2$  a weak instability at injection energy with  $dQi \lesssim 10^{-5}$  is found. The growth rate depends slightly on chromaticity but some growth is always predicted. Predictions for other accelerators are similar, with no instability showing up in the real machine. More work is needed to understand this but it is likely that synchrotron or betatron tune spread will Landau damp the higher order unstable modes.

Longitudinal instabilities at injection and during the ramp will not be a problem if the impedance is kept small enough. Since transition is not crossed the broad band impedance will be an issue only if the coherent tune shift is large enough to cause undamped coherent oscillations. These oscillations are not in themselves a problem, but will allow small parasitic resonances to drive unstable modes. Therefore, the broad band impedance is constrained by demanding that coherent dipole oscillations are damped by the synchrotron tune spread. This remains to be done.

Transverse instabilities at store are more interesting. Figure 36 shows the growth rates of the  $m = 0$  modes at the beginning of store. The most unstable mode has  $Im(\Delta Q) = 0.0025$ , which is significantly larger than the synchrotron tune. If this mode is present it must be actively damped.

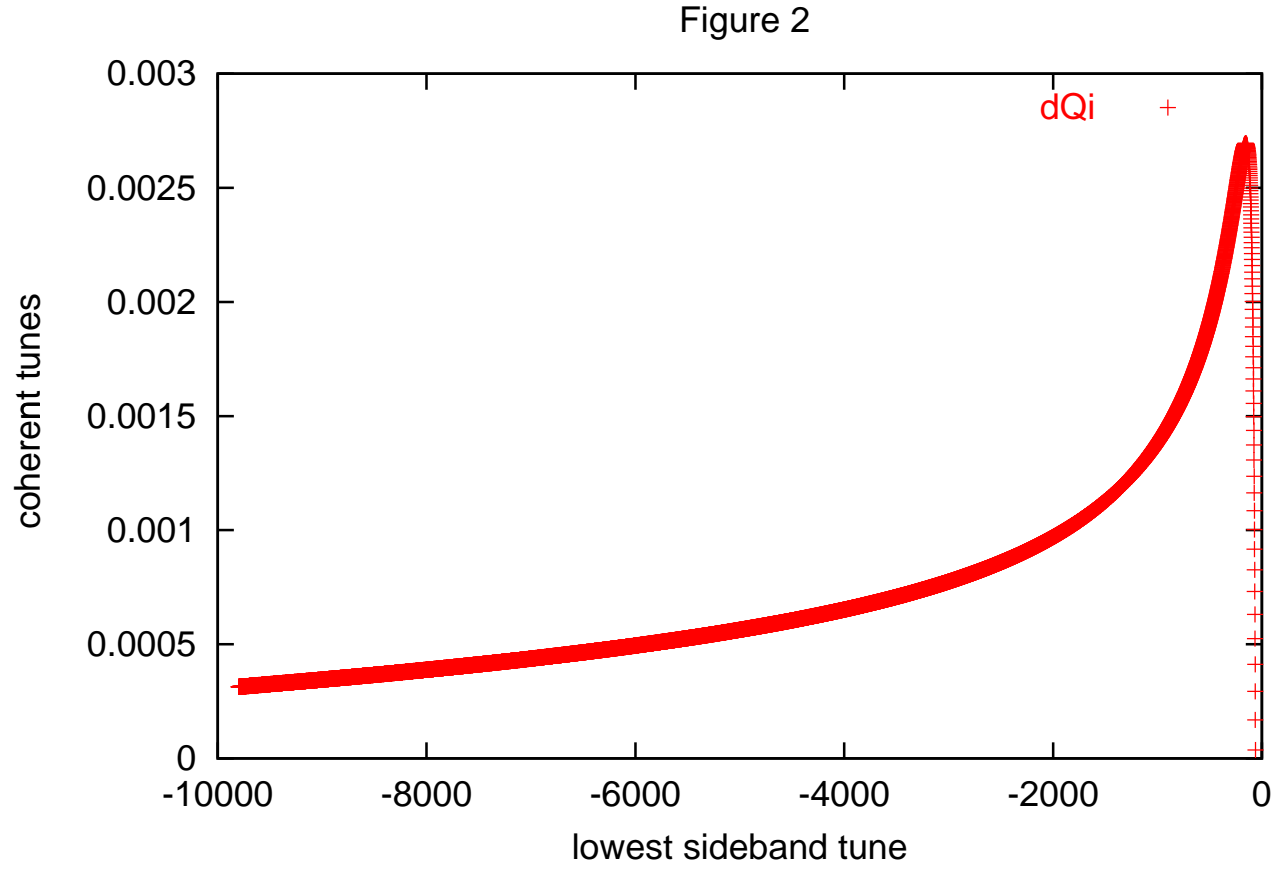


Figure 34: Imaginary part of unstable coherent tunes for  $m=0$  at 10 TeV versus observed frequency of lowest betatron sideband in units of the revolution frequency (1.29kHz). The characteristic damper frequency is 5kHz and gain corresponding to  $dQr = -0.4$  at the strongest damped sideband.

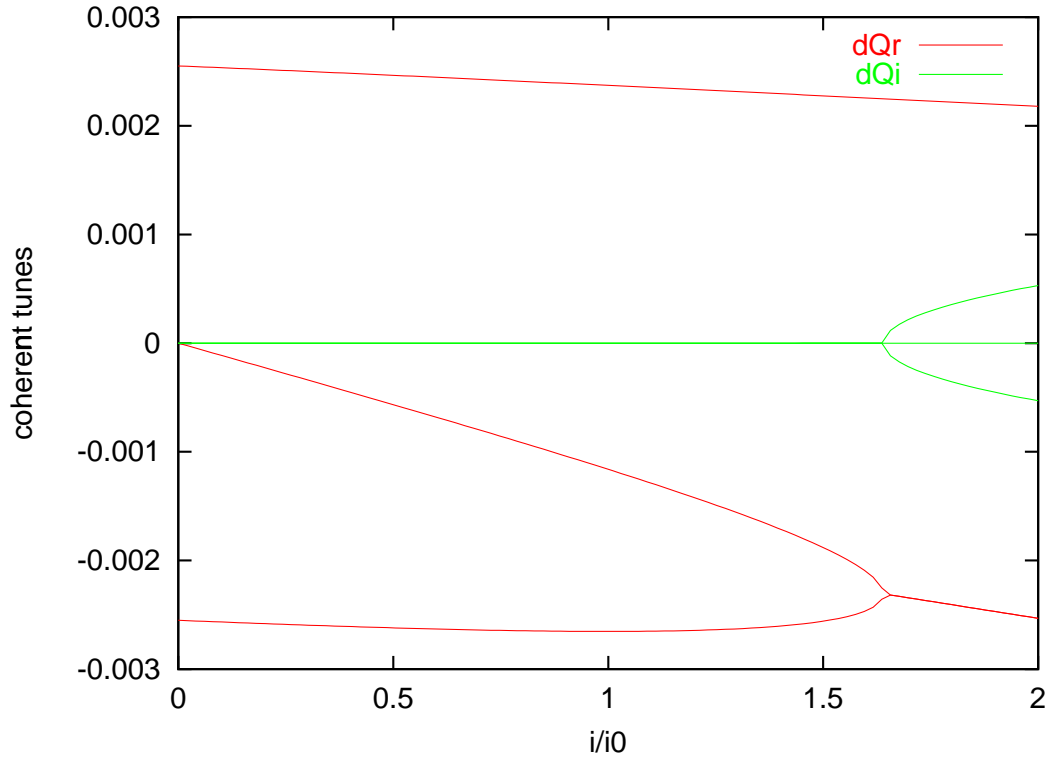


Figure 35: Growth rates for fast head-tail at 10 TeV versus bunch current in  $10^{10}$  protons.

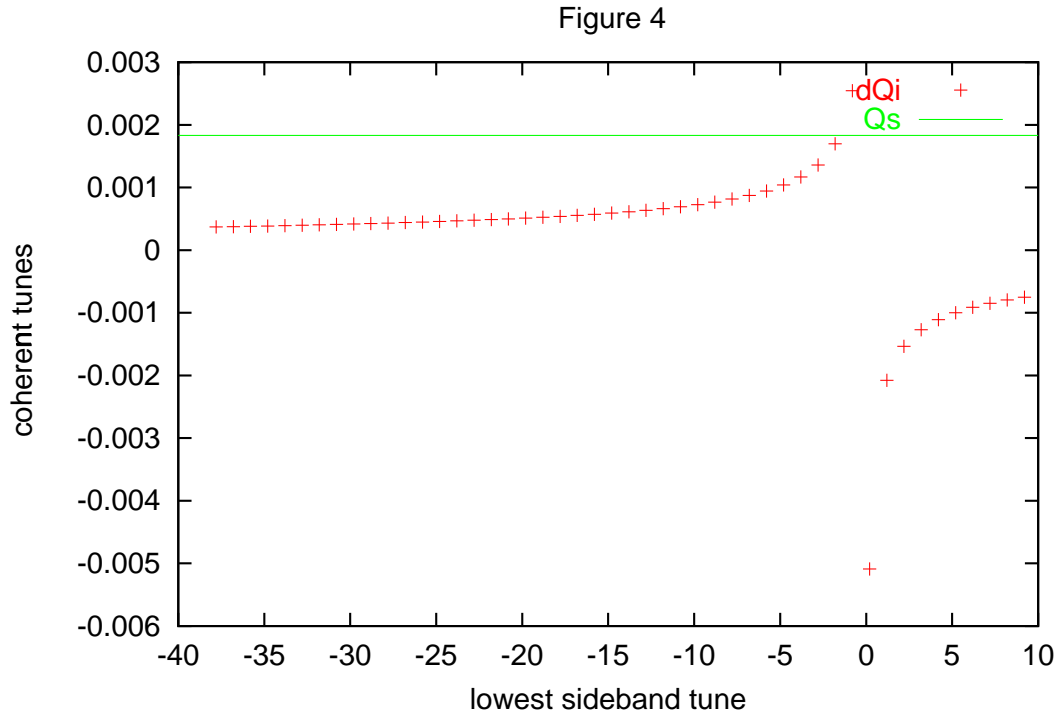


Figure 36: Imaginary part of unstable coherent tunes for  $m=0$  and 87.5 TeV versus observed frequency of lowest betatron sideband in units of the revolution frequency (1.29kHz). The horizontal line is the synchrotron tune for 200 MV/turn.

### 3.7 Synchrotron radiation (Trbojevic)

Proton beams in the VLHC emit synchrotron radiation just as electrons do in electron storage rings. An important advantage of synchrotron radiation in the high energy ring is that the significant damping stabilizes the beam dynamics, shrinks the emittances, enables flat beam collisions, and tends to make store performance independent of injection errors. On the other hand, disadvantages include a large power load to the cryogenic system, photon induced gas desorption, and the possibility of electron cloud instability.

The critical wavelength characterizing the synchrotron radiation spectrum in a dipole of bend radius  $\rho = 29.9$  km is

$$\lambda_c = \frac{4\pi\rho}{3\gamma^3} = 1.543 \text{ [Å]} \quad (53)$$

where  $\gamma = 9.33 \times 10^4$  is the Lorentz factor corresponding to the storage energy of  $E = 87.5$  TeV. Photons are emitted tangential to the proton path within a small angle  $\theta \sim 1/\gamma \approx 10 \text{ } \mu\text{rad}$ . The vast majority of photons (91%) have energies smaller than the critical energy, given by

$$E_c \text{ [keV]} = \frac{1.239}{\lambda_c \text{ [Å]}} = 8.03 \text{ [keV]} \quad (54)$$

Nonetheless, the critical energy divides the spectrum in half with respect to the dissipated power.

The energy loss per particle per turn is

$$U_0 = \frac{C_g E^4}{2\pi} C \langle G^2 \rangle = 15.3 \text{ [MeV]} \quad (55)$$

where  $C$  is the total circumference, the constant  $C_g = 7.783 \times 10^{-18} \text{ m GeV}^{-3}$  for protons, and  $G = 1/\rho$  is the dipole bending strength. Angle brackets  $\langle \rangle$  denote an average over the entire design trajectory circumference in the general case when there is more than one bend radius. However, the VLHC is isomagnetic – has only has one bend radius – and so

$$\langle G^n \rangle = \frac{1}{\rho^n} \quad (56)$$

The number of photons emitted per proton per turn is

$$N_\gamma = \frac{15\sqrt{3}}{8} \frac{U_0}{E_c} = 6188 \quad (57)$$

and so the total photon rate per unit length in a dipole is

$$\frac{dN}{ds} = 2.56 \times 10^{17} I = 1.76 \times 10^{16} \text{ [photons/(m s)]} \quad (58)$$

where the nominal beam current is  $I = 68.9$  mA. The total synchrotron power radiated in a single ring is

$$P = U_0 I = 1.05 \text{ [MW]} \quad (59)$$

for a two ring total of 2.1 MW.

The exponential damping times for the amplitudes of horizontal, vertical, and longitudinal oscillations are given by

$$\tau_{x,y,s} = T_0 / J_{x,y,s} \quad (60)$$

where the characteristic time  $T_0 = 2T_{rev}(E/U_0)$  is simply related to the revolution period,  $T_{rev}$ . Natural partition number values  $(J_x, J_y, J_s) = (1, 1, 2)$  are assumed. The equilibrium rms momentum width is

$$\left( \frac{\sigma_p}{p} \right)^2 = \frac{C_q \gamma^2}{J_s} \frac{\langle G^3 \rangle}{\langle G^2 \rangle} \quad (61)$$

while the natural *normalized* rms horizontal emittance is

$$\epsilon_x \equiv \gamma \frac{\sigma^2}{\beta} = \frac{C_q \gamma^3}{J_x} \frac{\langle G^3 H \rangle}{\langle G^2 \rangle} \quad (62)$$

where  $C_q = 2.087 \times 10^{-16}$  m and  $H$  is a property of the FODO cell optics

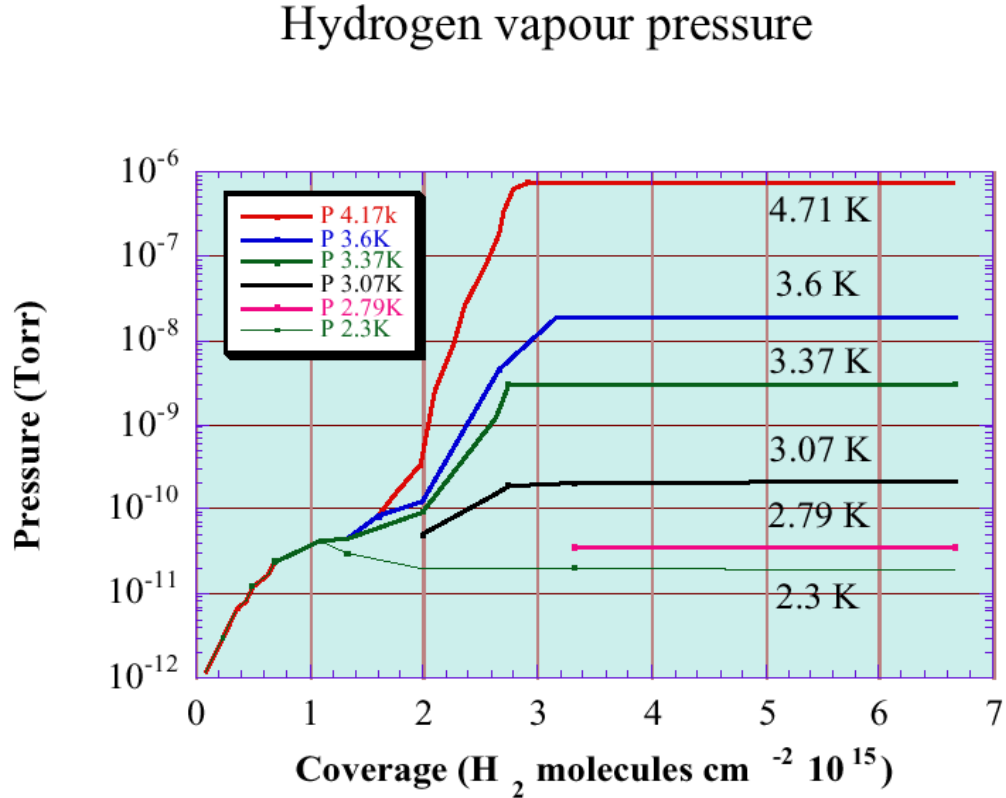
$$H = \gamma\eta^2 + 2\alpha\eta\eta' + \beta\eta'^2 \quad (63)$$

where  $\alpha$ ,  $\beta$ ,  $\gamma$ , and  $\eta$  are Twiss functions.

Note that  $U_0 \sim B\gamma^3$  and  $T_0 \sim 1/(B^2\gamma)$ , where  $B$  is the dipole field, independent of the lattice optics structure. The momentum width is also independent of the lattice structure, and scales like  $\sigma_p/p \sim \sqrt{B\gamma}$ . By contrast, the natural horizontal emittance depends strongly on the lattice, scaling like  $\epsilon_x \sim B^3 L^3$ , where  $L$  is the half length of a FODO cell. The *normalized* emittance is independent of energy!

Electron storage rings all operate with a room temperature beam environment. By contrast, when a significant number of photons are emitted in the cryogenic environment of a superconducting hadron collider, it is necessary to introduce a liner between the cold vacuum wall and the beam. This necessity was recognized even before the LHC design, as the result of experiments performed to study the photon stimulated desorption conditions expected at cryogenic temperatures in the SSC [15]. More refined experiments have been performed during the LHC design process [16].

The basic mechanism of gas desorption at the beam pipe or liner surface is electron excitation from the incident photons. These photons have enough energy to eject or excite even the inner shell electrons. There are several unwanted electron relaxation results at surfaces in the VLHC like ejected and secondary electrons, neutrals, and ion desorption. The “redistribution” of (mostly) hydrogen molecules continually enhances the background vacuum pressure in both the LHC and the VLHC, reducing the beam life time. Hydrogen molecules are physisorbed at the cold walls with a binding energy of less than 1 eV. The dependence of the hydrogen vapor pressure on the wall temperature is shown in Fig. 37.



C. Benvenuti, R. Calder

Figure 37: Hydrogen vapor pressure as a function of coverage and temperature.

The LHC is confronted with the real possibility of an electron cloud instability. When free electrons are present in the beam pipe, the electric field of the passing proton bunches can accelerate them to energies in the keV range.

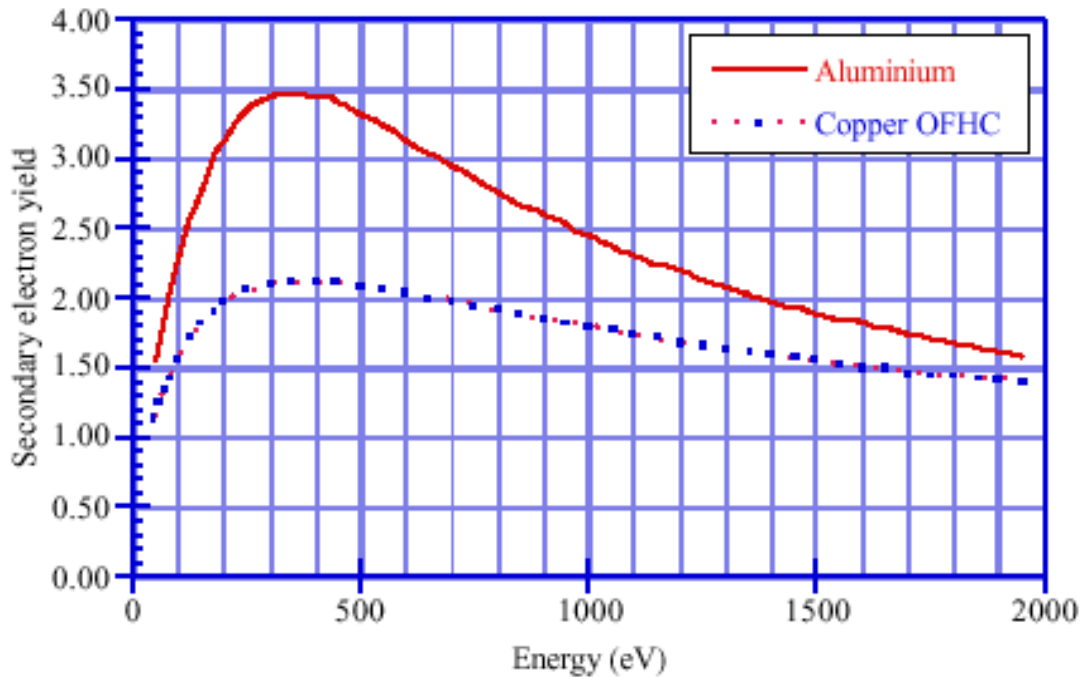


Figure 38: Yield of secondary electron as a function of energy of primary electrons.

They then hit the other side of the liner wall, creating secondary electrons which may be accelerated by a following bunch. An avalanche process can occur, leading to a large thermal beam load and even to beam loss. One important parameter, the secondary electron yield, determines the average number of secondary electrons per incident electron. It varies with the wall materials, surface conditions, and with the incident electron energy, as shown in Fig. 38. Another important parameter is the spacing between bunches. If the time between bunches is much larger than the typical time for electrons to travel between the two liner walls, then the avalanche process may be suppressed. The photon reflectivity of the liner or vacuum wall is another important parameter.

A dedicated VLHC workshop, *Synchrotron Radiation Effects in the VLHC*, was organized in September 2000, at Brookhaven National Laboratory, to discuss the operational impact of synchrotron radiation in both low and high field rings. Major conclusions from the workshop include:

1. A liner is necessary in both low and high field rings
2. Even with a liner, a significant pump-out time will be necessary to reach stable operating vacuum conditions. The hydrogen vapor pressure in the beam pipe must be less than  $\sim 10^{-10}$  Torr for beam lifetimes larger than 100 hours. The coverage of hydrogen molecules, and the vapor pressure, rise rapidly above cold bore temperatures of 3 K. If the cold bore temperature is larger than 3 K, then additional pump-out getter materials between the bore and the liner might be required.
3. Preliminary calculations show that the electron cloud instability could be serious if the number of protons per bunch is larger than  $2 \times 10^{10}$ . Fortunately this is more than a factor of 2 larger than the nominal population of  $N = 9 \times 10^9$ .
4. The power load from the synchrotron radiation to the cryogenic system can be reduced if it is possible to place a special “warm” photon stopper once every few dipoles.

### 3.8 Electron cloud instability (Zhang)

### 3.9 Energy deposition (Drees)

In a collider with beam energies  $E_{beam}$  of 87.5 TeV and a peak luminosity  $\mathcal{L}$  of  $2 \times 10^{34} cm^{-2} s^{-1}$  energy deposition from the particles created in pp collisions is significant and could eventually pose a problem for the superconducting magnets close to the IR.

The deposited energy on one side of the IR,  $E_d$ , in units of kW is given by:

$$E_d = N \times 0.5 \times E_{fwd}, \quad (64)$$

where  $N$  corresponds to the number of collisions per hour and  $E_{fwd}$  to the total energy of particles in forward direction in units of kWh. In general,  $N$  is determined by:

$$N = \sigma_{tot} \times \mathcal{L} \times 3600. \quad (65)$$

Table 21 shows a list of the dominant processes and their cross sections at  $\sqrt{s} = 175000$  GeV according to the high energy event generator PYTHIA [26]. While the first 2 processes do not contribute exclusively to energy deposition in forward direction, the latter four do, accumulating to a “forward” cross section of 66 mb.

index	subprocess	$\sigma$ (mb)
1	$f + g \rightarrow f + g$	20.9
2	$g + g \rightarrow g + g$	63.2
3	Elastic scattering	35.9
4	Single diffractive (XB)	8.2
5	Single diffractive (AX)	8.2
6	Double diffractive	13.7

Table 21: Cross sections of the dominant processes at 175.0 TeV collisions (PYTHIA).  $f$  and  $g$  correspond to fermion and gluon respectively.

The elastic scattering and diffraction cross sections are reflected in the pattern in fig. 39 depicting high energy tracks only at small polar angles  $\Theta$ . In fact, PYTHIA predicts about 40% of all collisions with basically all energy, i.e. more or less the incoming protons, distributed in forward direction.

These events are of particular interest for us in cases when they have scattering angles smaller than the apex angle of the D1 magnets 30 m downstream of the IR. Under this condition the charged collision products are bent in the dipole field of the D1 magnets and contribute eventually to the energy deposition in the down stream IR quadrupoles Q1A and Q1B. Fig. 40 shows the energy distribution of charged and uncharged tracks with a polar angle  $\Theta < \Theta_{apex}$  with  $\Theta_{apex} = 0.00042$  rad. These tracks belong to an overall sample of 1000 generated PYTHIA events. The continuum of the charged particle energy distribution (lower left plot in fig 40) has a mean of 76360 GeV. The distribution peaks at  $2 \times E_{beam}$ .

The approximate number of collision particles hitting the IR dipoles and quadrupoles can be estimated by neglecting the uncharged particles, which aren't affected by the magnetic field of the D1 dipoles, but taking into account particles with small angles emerging from subprocesses 1 and 2 in Tab. 21. Assuming a mean total energy of 76 TeV of all charged particles contained within the beam pipe for 75% of the collisions and about 175 TeV for the remaining 25% an upper limit of 24 kW energy deposition on either side of the IR can be derived. However, this energy deposition is spread over a certain distance since the point where the particles hit the wall of the beam pipe depends on both, incoming angle and particle energy. For effective collimation or any other counter measure this has to be studied with more detail taking into account the machine lattice and magnet transfer functions.

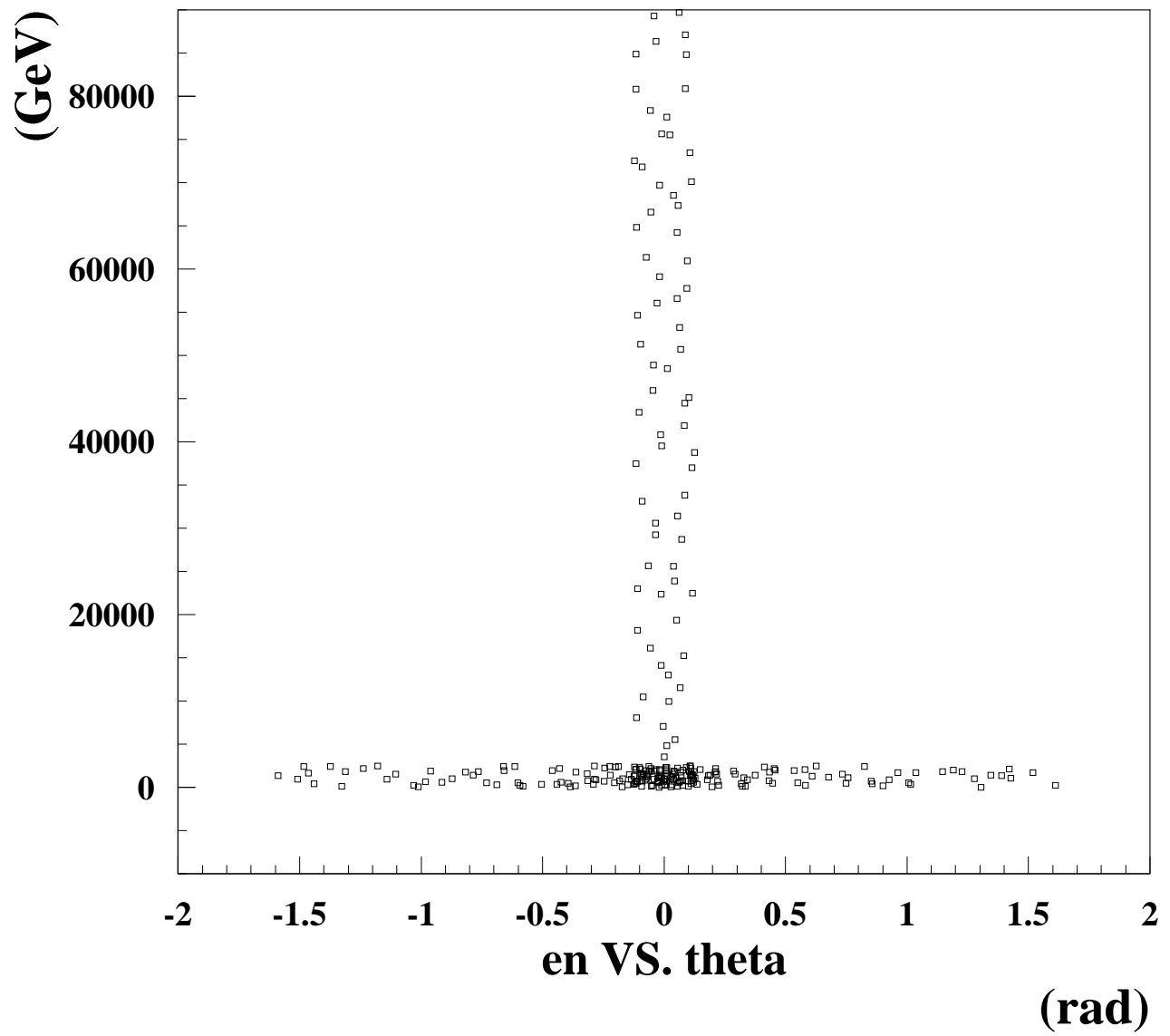
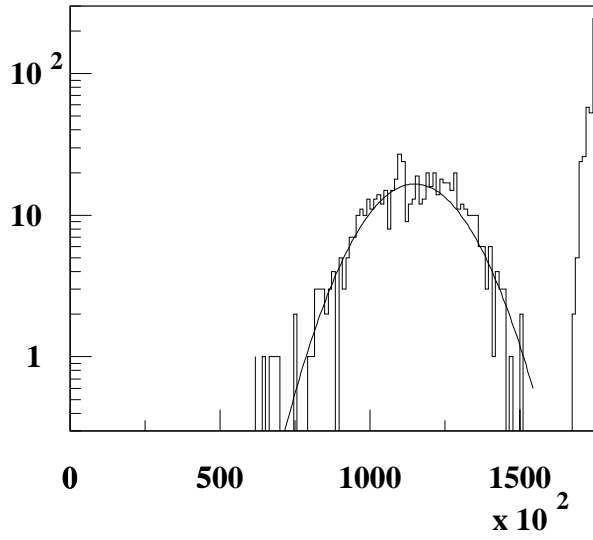
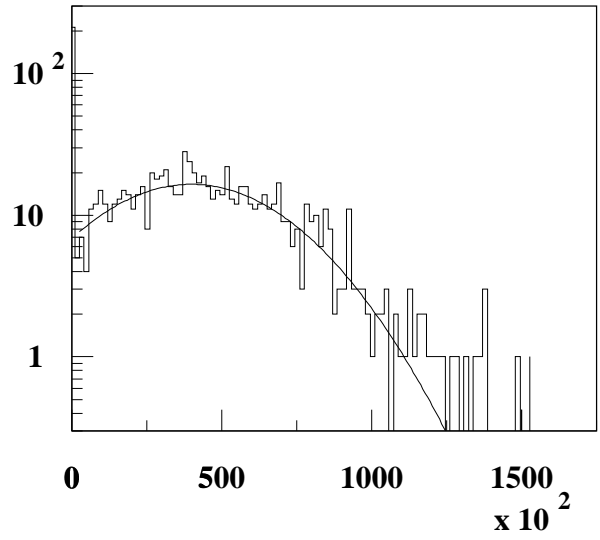


Figure 39: The energy of stable final state particles as a function of polar angle  $\theta$  (PYTHIA).

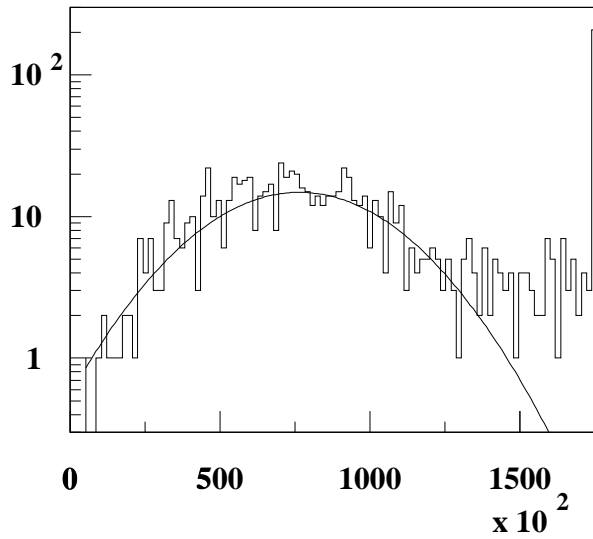
# forward energy distributions



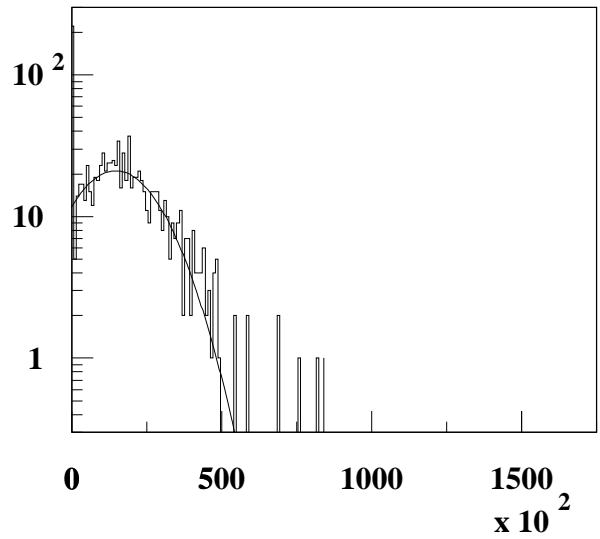
**all particles (GeV)**



**uncharged particles (GeV)**



**charged particles (GeV)**



**negative charged particles (GeV)**

Figure 40: Energy distribution of charged and uncharged tracks in forward direction in collisions at  $\sqrt{s} = 175000$  GeV (PYTHIA).

### 3.10 Parameter tables

Circumference, $C$	233.037	km
Average arc radius	35.0	km
Half cell length, $L_{hc}$	135.486	m
Half cell bend angle	3.875	mrاد
Half cell count	1720	
Half cell harmonic	24	
Bunch spacing (53.1 MHz)	5.645	m
Number of buckets	41280	
Phase advance per cell	90.0	deg
Revolution frequency	1.286	kHz
Harmonic number	371520	
RF frequency ( $9 \times 53.1$ )	478.0	MHz

Table 22: Fundamental lattice parameters common to both low and high field rings.

<b>Module</b>	Arc	DS	IA	DM8	IR	DM	X	DM	IR	DM8	IA	DS
$L/L_{hc}$	780	3	10	8	12	6	2	6	12	8	10	3

Table 23: Sequence of optical modules around half of the VLHC (mnemonic version).

MODULE	ALIAS	$L/L_{hc}$	COMMENT
Dispersion Suppressor	DS	3	
Injection/Abort straight	IA	10	
Dispersion Module	DM8	8	contains 2 arc half cells
Interaction Region	IR	12	
Dispersion Module	DM	6	
Crossing “straight”	X	2	
Dispersion Module	DM	6	
Interaction Region	IR	12	
Dispersion Module	DM8	8	contains 2 arc half cells
Injection/Abort straight	IA	10	
Dispersion Suppressor	DS	3	
Utility total		80	
Arc		780	
GRAND TOTAL		1720	2 arcs plus 2 utilities

Table 24: Sequence of optical modules in the on-site utility region of the VLHC.

Storage energy, $E$	87.5	TeV
Peak luminosity, $L_{max}$	$2 \times 10^{34}$	$\text{cm}^{-2}\text{s}^{-1}$
Total cross section at store	$1.5 \times 10^{-25}$	$\text{cm}^2$
Collision debris power, per IP	84	kW
Dipole field at storage	9.765	T
Number of interaction points	2	
Distance from IP to first magnet	30	m
Injection energy	10	TeV
Fill time	30	s
Acceleration time	2000	s
Transverse emittance, rms (inject)	1.5	$\mu\text{m}$
Longitudinal emittance, rms (inject)	2.0	eV-s
Bunch spacing (53.1 MHz)	5.645	m
	18.8	ns
Initial bunch intensity, $N$	$9 \times 10^9$	
Number of buckets,	41280	
Number of bunches, $M$	37152	
Fraction of buckets filled	90	%
Protons per beam	3.34	$10^{14}$
Beam current	68.9	mA
Collision beta horz, $\beta_x^*$	3.7	m
Collision beta vert, $\beta_y^*$	0.37	m
Natural transverse emittance (H)	.0397	$\mu\text{m}$
Equilibrium emittance (H) $\epsilon_x$	$\sim 0.20$	$\mu\text{m}$
Equilibrium emittance (V) $\epsilon_x$	$\sim 0.02$	$\mu\text{m}$
Equilibrium emittance ratio, $\kappa$	0.1	
Natural RMS momentum width	$5.5 \times 10^{-6}$	

Table 25: Nominal parameters for stores in the high field ring.

INJECTION		
Emittance, rms (H and V)	1.5	$\mu\text{m}$
Momentum width, rms	233.1	$10^{-6}$
Arc bunch size (betatron)	751	$\mu\text{m}$
Arc bunch size (dispersion)	330	$\mu\text{m}$
RF voltage	50.0	MV
Longitudinal rms emittance	2.0	eV-s
Longitudinal beta	351	m
Bunch length, rms	81.9	mm
Synchrotron tune	.00280	
Synchrotron frequency	3.60	Hz
STORE BEGINNING		
Emittance, rms (H and V)	1.5	$\mu\text{m}$
Momentum width, rms	64.8	$10^{-6}$
Arc bunch size (betatron)	254	$\mu\text{m}$
Arc bunch size (dispersion)	92.0	$\mu\text{m}$
Full crossing angle	65.9	$\mu\text{rad}$
RF voltage	200	MV
Longitudinal rms emittance	2.0	eV-s
Longitudinal beta	520	m
Bunch length, rms	33.7	mm
Synchrotron tune	.00189	
Synchrotron frequency	2.44	Hz
EARLY PLATEAU (Flat beams)		
Beam-beam parameter	.008	
Emittance, rms (H)	.20	$\mu\text{m}$
Emittance, rms (V)	.02	$\mu\text{m}$
Momentum width, rms	50.0	$10^{-6}$
Arc bunch size (betatron)	32.2	$\mu\text{m}$
Arc bunch size (dispersion)	71.0	$\mu\text{m}$
IP bunch size (H)	2.89	$\mu\text{m}$
IP bunch size (V)	.29	$\mu\text{m}$
Full crossing angle	6.5	$\mu\text{rad}$
RF voltage	200	MV
Longitudinal rms emittance	1.191	eV-s
Longitudinal beta	520	m
Bunch length, rms	26.0	mm
Synchrotron tune	.00189	
Synchrotron frequency	2.44	Hz

Table 26: Store parameters, including longitudinal and RF.

Energy loss per turn, $U_0$	15.3	MeV
Revolution period, $T_{rev}$	.778	ms
Damping time, $T_0$	2.48	h
Synch. rad. power, per beam $P$	1.05	MW
Dipole linear heat load	5.6	W/m
Stored energy, per beam $U$	4.7	GJ

Table 27: Synchrotron radiation related parameters.

Horizontal tune	218.19	
Vertical tune	212.18	
Transition gamma	194.13	
Slip factor	$2.653 \times 10^{-5}$	
Maximum arc beta	459	m
Maximum arc dispersion	1.42	m
Rigidity at injection	$3.336 \times 10^4$	Tm
Rigidity at store	$2.919 \times 10^5$	Tm
Vertical $\beta^*$ (store)	0.37	m
Horizontal $\beta^*$ (store)	3.7	m
Maximum $\beta$ , injection	.614	km
Maximum $\beta_{max}$ , store	10.6	km

Table 28: Short list of some high field lattice parameters.

DIPOLE		
Field at injection	1.116	T
Field at store	9.765	T
Bend radius	29.887	km
Coil full width	40	mm
Liner full width	20	mm
Vertical bore separation	.29	m
Stored energy (2 bores)	828	kJ/m
CORRECTORS		
Corrector magnetic length	1.0	m
Dipole corrector max strength	4.0	Tm
Skew quad max strength	141	T
Sextupole max strength	6000	T/m
ARC CELLS		
Half cell harmonic	24	
Half cell length	135.486	m
Half cell bend angle	3.875	mrاد
Half cell count	1568	
Dipoles per half cell	7	
Dipole count, total	10976	
Dipole magnetic length	16.546	m
Dipole fill factor	85.5	%
Quad magnetic length	8.066	m
Quad field gradient	385.4	T/m
DISPERSION SUPPRESSOR CELLS		
Half cell harmonic	18	
Half cell length	101.614	m
Half cell bend angle	2.583	mrاد
Half cell count	80	
Dipoles per half cell	5	
Dipole count, total	400	
Dipole magnetic length	15.443	m
Dipole fill factor	76.0	%
Quad magnetic length	10.775	m
Quad field gradient (QD1)	288.7	T/m
Quad field gradient (QF2)	376.2	T/m
Quad field gradient (QD3)	281.9	T/m
Quad field gradient (QF4)	390.2	T/m

Table 29: Arc and dispersion suppressor magnet and cell parameters.

### 3.11 Magnet reference harmonics

The expansion for the field error in a dipole magnet is written in terms of coefficients  $(b_n, a_n)$  as

$$\Delta(B_y + iB_x) = B_0 10^{-4} \sum_{n=1} (b_n + ia_n) \left( \frac{x + iy}{r_0} \right)^n \quad (66)$$

where  $B_0$  is the main dipole field and  $r_0 = 10$  mm is the reference radius in all cases. Similarly, for a quadrupole

$$\Delta(B_y + iB_x) = G_0 r_0 10^{-4} \sum_{n=2} (b_n + ia_n) \left( \frac{x + iy}{r_0} \right)^n \quad (67)$$

where  $G_0$  is the main quadrupole field gradient. In the following tables, for each set of magnets,  $b_n$  ( $a_n$ ) is the mean or systematic value of the normal (skew) harmonic,  $\Delta(b_n)$  is the uncertainty of the systematic normal harmonic, and  $\sigma(b_n)$  is the standard deviation of the normal harmonic. The convention in which  $n = 2$  is sextupole is used throughout.

n	$b_n$	$\Delta b_n$	$\sigma(b_n)$	$a_n$	$\Delta a_n$	$\sigma(a_n)$
1		.5	1.2	.005	.5	1.2
2	-2.0	1.0	.85		.3	.85
3		.2	.3	-.001	.2	.3
4	-.5	.2	.12		.2	.12
5			.05	-.002		.05
6	-.001		.02			.02
7			.008	.011		.008
8	-.046		.005			.005
9			.001	.003		.001

n	$b_n$	$\Delta b_n$	$\sigma(b_n)$	$a_n$	$\Delta a_n$	$\sigma(a_n)$
1		.5	1.2		.5	1.2
2		.5	.6		.3	.6
3		.2	.3	-.001	.2	.3
4	-.001	.05	.1		.05	.1
5			.05	-.002		.05
6	-.001		.02			.02
7			.008	.011		.008
8	-.046		.005			.005
9			.001	.003		.001

Table 30: Arc dipole body harmonics, v1.0. At injection with  $B = 2$  T (top), and at storage with  $B = 10$  T (bottom).

The injection energy dropped from the 20 TeV value used for v1.0 harmonics to 10 TeV. The injection field reduces from 2.28 T to 1.14 T and injection field gradient from 90 T/m to 45 T/m. The components of field harmonics related to the coil magnetization effect at injection have been checked and corrected if necessary.

n	$b_n$	$\Delta b_n$	$\sigma(b_n)$	$a_n$	$\Delta a_n$	$\sigma(a_n)$
2		.75	1.875		.75	1.875
3	.004	.5	.875		.5	.875
4		.125	.375		.125	.375
5	-2.5	.25	.25		.125	.25
6			.075			.075
7	-.0035		.025			.025
8			.025			.025
9	.1	.025	.0125			.0125

n	$b_n$	$\Delta b_n$	$\sigma(b_n)$	$a_n$	$\Delta a_n$	$\sigma(a_n)$
2		.75	1.875	.175	.75	1.875
3	.03	.50	.875		.5	.875
4		.125	.375		.125	.375
5	.03	.075	.2		.075	.2
6			.075			.075
7	-.0035		.025			.025
8			.025			.025
9	-.004	.025	.0125			.0125

Table 31: Arc quadrupole body harmonics, v1.0. At injection with  $G = 80$  T/m (top), and at storage with  $G = 400$  T/m (bottom).

n	$b_n$	$\Delta b_n$	$\sigma(b_n)$	$a_n$	$\Delta a_n$	$\sigma(a_n)$
1		.5	1.2		.5	1.2
2	-2.0	1.0	.85		.3	.85
3		.05	.35		.05	.35
4	.5	.2	.12		.2	.12
5	-.006	.006	.05		.002	.05
6	-.004	.007	.02			.02
7	.015	.015	.008	.01	.005	.008
8	-.065	.065	.005			.005
9	-.006	.006	.001	.002	.001	.001

n	$b_n$	$\Delta b_n$	$\sigma(b_n)$	$a_n$	$\Delta a_n$	$\sigma(a_n)$
1		.5	1.2		.5	1.2
2		.5	.6		.3	.6
3		.05	.3		.05	.3
4		.05	.1		.05	.1
5	-.006	.006	.05		.002	.05
6	-.004	.007	.02			.02
7	.015	.015	.008	.01	.005	.008
8	-.065	.065	.005			.005
9	-.006	.006	.001	.002	.001	.001

Table 32: Arc dipole body harmonics, v1.1. At injection with  $B = 1.14$  T (top), and at storage with  $B = 10$  T (bottom).

n	$b_n$	$\Delta b_n$	$\sigma(b_n)$	$a_n$	$\Delta a_n$	$\sigma(a_n)$
2		.25	1.875		.25	1.875
3		.25	.875		.25	.875
4		.125	.375		.125	.375
5	-1.25	.25	.25		.125	.25
6			.075			.075
7	-.004		.025			.025
8			.025			.025
9	.075	.025	.013		.013	.0125

n	$b_n$	$\Delta b_n$	$\sigma(b_n)$	$a_n$	$\Delta a_n$	$\sigma(a_n)$
2		.5	1.875	.175	.5	1.875
3		.25	.875		.25	.875
4		.125	.375		.125	.375
5	.025	.025	.2		.025	.2
6			.075			.075
7	-.0035		.025			.025
8			.025			.025
9	-.004	.003	.0125			.0125

Table 33: Arc quadrupole body harmonics, v1.1. At injection with  $G = 45$  T/m (top), and at storage with  $G = 400$  T/m (bottom).

n	$b_n$	$\Delta b_n$	$\sigma(b_n)$	$a_n$	$\Delta a_n$	$\sigma(a_n)$
2		2	2	3	3	1
3	2	2	1		1	1
4		1	1	1.5	1.5	1
5	1	1	.5		1	.2
6		.1	.1	.5	.5	.5
7	.5	.5	.1		.2	.1
8		.1	.1	.3	.3	.1
9	.5	.5	.1		.1	.1

Table 34: Interaction region quadrupole integrated harmonics for Q1 and Q2, v1.0.

## 4 GROUND MOTION AND EMITTANCE GROWTH (Shiltsev)

We have measured the slow ground motion in 300-ft deep dolomite Conco mine in Aurora, IL, about 3 miles west of Fermilab. The goal of the studies is to record and analyze vertical ground motion in 8 points separated by 30 meters over a time interval of about 1 year. The experiment in Aurora mine started in October 2000. The first data reveal that dolomite mine motion is rather small and can be described by the ATL law with coefficient of  $A = (6.8 \pm 2.7) \times 10^{-7} \text{ } \mu\text{m}^2/\text{m/s}$  [3]. The resulting maximum orbit distortion in the VLHC which will be caused by that is of the order of  $9 \text{ mm}/\sqrt{\text{year}}$ .

The only drawback of the Aurora mine experiment is too few sensors that limit statistics for studies of spatial correlations. Therefore, a system with about 20 sensors is needed, and long term measurements should be repeated in the larger scale. Analytical/computer studies of the slow ground motion effects and orbit correction system and procedures must be performed.

Turn-to-turn dipole magnetic field fluctuations and vibration of quadrupole magnets are of concern, because they can excite coherent beam motion. If the motion is not corrected over the *decoherence time* of about  $1/\xi_{\text{beam-beam}} \approx 1000$  turns, then the coherent motion will be converted into transverse emittance increase and can cause substantial emittance growth over about 10 hours of the store. So far, experimentally measured high-frequency ground or magnet vibrations do not pose a big problem for VLHC [5]. Nevertheless, more detailed analysis on how the lattice may affect the tolerances is needed. For example reference [4] claims that tolerances on vibration amplitude in a lattice with combined function magnets is about 3 times the tolerances in a separated function FODO lattices.

In 1999 we carried out experimental studies of high-frequency magnetic field fluctuations in the Tevatron superconducting dipole magnet and found that effective rms  $dB/B \approx 10^{-10}$  that is about 10 times the tolerance for the VLHC, i.e. that might cause emittance doubling after about 6 minutes. The measurements have to be repeated in the VLHC dipole prototypes. Again, we need to analyze and perform computer simulations for lattices with separated and combined function magnets.

Suppression of the emittance growth can be provided by low noise feedback. The first analysis of the FB is presented in [6]. The system has to have sub-micron equivalent input noise. Design and test of such a system at the Tevatron is a very desired VLHC beam physics R&D.

## References

- [1] P. Limon (editor), *VLHC Feasibility Study*, FNAL ??, May 2001.
- [2] J.P. Koutchouk, *The LHC Dynamic Aperture*, PAC 1999.
- [3] V. Shiltsev, *Proc. ICFA Workshop on Ground Motion*, Nov. 2000, SLAC;  
<http://www-project.slac.stanford.edu/lwshp/GM2000>
- [4] V. Shiltsev, FNAL TM-1987, 1996.
- [5] B. Baklakov et al, PRST Accel. Beams, 031001, 1998.
- [6] A. Burov et al, *Beam Stability Issues in a Very Large Hadron Collider*, p. 194 NIMA 450, 2000.
- [7] J. Wei, *Intra-beam scattering scaling for Very Large Hadron Colliders*, BNL C-A/AP/38, Feb. 2001.
- [8] S. Peggs, F. Dell, *Tolerable systematic errors in Really Large Hadron Colliders*, Snowmass, 1996.
- [9] S. Peggs, M. Harrison, F. Pilat, M. Syphers, *Flat beams in a 50 TeV hadron collider*, Vancouver PAC 97, 1997.
- [10] S. Peggs et al, *Lattices for a high-field 30 TeV hadron collider*, Snowmass, 1996.
- [11] J. Wei, S. Peggs, *Interaction region analysis for a high-field hadron collider*, Snowmass, 1996.
- [12] S. Peggs et al, *Lattice optimization for a Really Large Hadron Collider*, Barcelona EPAC 96, 1996.
- [13] W. Fischer, *An Experimental Study on the Long-term Stability of Particle Motion in Hadron Storage Rings*, PhD thesis Hamburg University, DESY 95-235 (1995) and CERN SL/96-10 (AP), 1996.
- [14] W. Fischer, M. Giovannozzi and F. Schmidt, *Dynamic Aperture Experiment at a Synchrotron*, Phys. Rev. E, Vol. 55, Number 3, p. 3507, 1997.
- [15] Stimulated desorption experiments??
- [16] Stimulated desorption experiments??
- [17] Condon & Odishaw, *Handbook of Physics*, pg 4-72, 1967.
- [18] Gary McIntyre, private communication.
- [19] J.M. Wang, SLAC summer school, 1985.
- [20] J. Marriner, FNAL tech note, September, 1997.
- [21] M. Blaskiewicz, W.T. Weng, Phys. Rev. E, Vol 50, # 5, p 4030, 1994.
- [22] Y.H. Chin, CERN/LEP-TH/88-05, 1988.
- [23] A. Chao, *Physics of Collective Beam Instabilities in High Energy Accelerators*, John Wiley and Sons, 1993, and references therein.
- [24] S. Peck, , Snowmass, 198n.
- [25] E. Keil, R. Talman, .....
- [26] T. Sjostrand, *PYTHIA 5.7 and JETSET 7.4, Physics and Manual*, Computer Physics Commun. 82 (1994) 74.